Geochimica et Cosmochimica Acta 360 (2023) 207–230

Contents lists available at ScienceDirect

Geochimica et Cosmochimica Acta

journal homepage: www.elsevier.com/locate/gca

Formation and transformation of Fe(III)- and Ca-precipitates in aqueous solutions and effects on phosphate retention over time

Ville V. Nenonen [a,b], Ralf Kaegi [a], Stephan J. Hug [a], Jörg Göttlicher [c], Stefan Mangold [c], Lenny H.E. Winkel [a,b], Andreas Voegelin [a,*]

[a] Eawag, Swiss Federal Institute of Aquatic Science and Technology, Überlandstrasse 133, CH-8600 Dübendorf, Switzerland
[b] ETH Zurich, Institute of Biogeochemistry and Pollutant Dynamics, Universitätstrasse 16, CH-8092 Zürich, Switzerland
[c] Karlsruhe Institute of Technology, Institute for Photon Science and Synchrotron Radiation, Hermann-von-Helmholtz Platz 1, D-76344 Eggenstein-Leopoldshafen, Germany

ARTICLE INFO

Associate editor: Elizabeth Herndon

Keywords:
Iron
Phosphate
Calcium
Oxidation
Precipitation
Aging
Transformation
Groundwater
Eutrophication

ABSTRACT

Exfiltration of anoxic phosphate-rich groundwater into surface water leads to the oxidation of dissolved Fe(II) and the formation of Fe(III)-precipitates that can retain phosphate (PO_4) and thereby attenuate eutrophication. Fresh Fe(III)-precipitates transform into more stable phases over time, and retained PO_4 may be released again. In parallel, CO_2 outgassing can promote the formation of Ca-phosphates or -carbonates that also sequester PO_4. In laboratory experiments, we studied the effects of Mg, Ca, silicate (SiO_4) and PO_4 on these processes. Fresh Fe(III)-precipitates were formed in bicarbonate-buffered aqueous solutions at pH ~ 7.0 via the oxidation of 0.5 mM Fe(II) in the presence of 0.15 or 0.025 mM PO_4, at Mg or Ca concentrations of 0, 0.4, 1.2 or 4 mM and in the absence or presence of 0.5 mM SiO_4. After CO_2 outgassing, the suspensions were allowed to age for 100 d at pH ~ 8. Changes in the composition and structure of Fe(III)- and Ca-precipitates over time were probed with spectroscopic and microscopic techniques and were linked to variations in the retention of PO_4. The oxidation of Fe(II) led to effective PO_4 removal via the formation of Fe(III)-precipitates that consisted of amorphous (Ca-)Fe(III)-phosphate ((Ca)FeP), ferrihydrite (Fh) and, in SiO_4-free treatments, lepidocrocite (Lp). During aging, FeP and Fh that had formed in the absence of Mg, Ca and SiO_4 rapidly and nearly completely transformed into Lp. Via effects on molecular- and nanoscale precipitate structure, Mg slowed down FeP transformation into Fh, stabilized Fh, and decreased the crystallinity of Lp (in SiO_4-free suspensions), Ca stabilized CaFeP against transformation into Fh, and SiO_4 stabilized Fh and (Ca)FeP. Core/shell CaFeP/Fh particles formed in electrolytes that contained Ca and SiO_4 hardly transformed within 100 d. Calcite only formed at low dissolved PO_4 concentrations and, by incorporation of PO_4, contributed to PO_4 retention. Higher levels of dissolved PO_4 inhibited calcite formation but could induce Ca-phosphate precipitation. Differences in precipitate formation and transformation pathways and kinetics were reflected in the extents of PO_4 release over the 100-d aging period, ranging from rapid release of 77% of the total PO_4 in the treatment without Mg, Ca and SiO_4 at 0.15 mM total PO_4 to slow release of only 0.1% of the total PO_4 at initial concentrations of 4 mM Ca, 0.5 mM SiO_4, and 0.025 mM PO_4. In summary, this study reveals the conditions and the extents and timescales over which Fe(III)- and Ca-precipitates form and transform and how these processes affect PO_4 immobilization in near-neutral natural waters. The detailed new insights into the coupling between Fe(III)- and Ca-precipitate formation and into the interdependent effects of Mg, Ca, SiO_4 and PO_4 are not only relevant with respect to PO_4 but also with respect to the cycling of trace elements in natural and engineered systems.

1. Introduction

Phosphorus (P) is an essential and often growth-limiting nutrient. In agriculture, P fertilization ensures high crop yields and food production safety. The release of P from agricultural soils into surface waters, on the other hand, is one of the main causes for the eutrophication and deterioration of aquatic ecosystems (Smith et al., 1999; Conley et al., 2009a; Conley et al., 2009b). Due to the high affinity of P as phosphate (PO_4) for

* Corresponding author at: Eawag, Swiss Federal Institute of Aquatic Science and Technology, Überlandstrasse 133, CH-8600 Dübendorf, Switzerland.
E-mail address: andreas.voegelin@eawag.ch (A. Voegelin).

https://doi.org/10.1016/j.gca.2023.09.004
Received 20 April 2023; Accepted 6 September 2023
Available online 7 September 2023

iron (Fe), the cycling of P in environmental systems is closely coupled to the cycling of Fe. At anoxic–oxic boundaries, for example sites of anoxic groundwater exfiltration into surface waters, the oxidation of dissolved Fe(II) leads to the formation of amorphous or poorly crystalline Fe(III)-precipitates (Griffioen, 2006; Roberts et al., 2007; Voegelin et al., 2010; Baken et al., 2016; van der Grift et al., 2016). These Fe(III)-precipitates exhibit a high sorption capacity for oxyanions and metal cations, and their formation therefore influences the fate of PO_4 and other nutrients and contaminants (Taylor and Konhauser, 2011; Kappler et al., 2021). The formation of Fe(III)-precipitates and impacts on PO_4 cycling have been studied with respect to various types of anoxic/oxic boundaries, including redoxclines in lake water columns and sediments (Hupfer and Lewandowski, 2008; Kleeberg et al., 2013; Cosmidis et al., 2014), estuarine and marine sediments (Hyacinthe and Van Cappellen, 2004; Paytan and McLaughlin, 2007; Mort et al., 2010; Kraal et al., 2012), brackish seawater (Gunnars et al., 2002), or sites of anoxic groundwater exfiltration into surface waters (Slomp and Van Cappellen, 2004; Griffioen, 2006; Roberts et al., 2007; Meinikmann et al., 2015; Baken et al., 2016; van der Grift et al., 2016).

The oxidation of dissolved Fe(II) in water at near-neutral pH induces the polymerization and precipitation of Fe(III). Common inorganic solutes in natural waters, including PO_4, magnesium (Mg), calcium (Ca), and silicate (SiO_4) influence these processes and thereby determine the structure of the forming solids and the extent to which solutes such as PO_4 are co-precipitated (Schwertmann and Thalmann, 1976; Carlson and Schwertmann, 1981; Mayer and Jarrell, 2000; Kaegi et al., 2010; Voegelin et al., 2010; van Genuchten et al., 2014a; van Genuchten et al., 2014b; Senn et al., 2015; Kraal et al., 2019). In the absence of interfering solutes in natural bicarbonate-buffered water, the oxidation of Fe(II) leads to predominant formation of lepidocrocite (Lp) (Schwertmann and Thalmann, 1976; Schwertmann and Taylor, 1979). SiO_4 at molar levels above ~0.05 Si/Fe promotes the formation of ferrihydrite (Fh) instead of Lp (Schwertmann and Thalmann, 1976; Carlson and Schwertmann, 1981; Senn et al., 2015). In aqueous solutions with an initial molar P/Fe ratio $(P/Fe)_{init}$ above a critical threshold $(P/Fe)_{crit}$ of ~0.5 (specific value close to the molar (P/Fe) of (Ca)FeP in the respective electrolyte), Fe(II) oxidation leads to the exclusive formation of amorphous Fe(III)-phosphate (FeP) (Voegelin et al., 2010; Châtellier et al., 2013; Voegelin et al., 2013; van der Grift et al., 2016). In Ca-containing water, amorphous Ca-Fe(III)-phosphate (CaFeP) with increased PO_4 uptake per Fe and enhanced degree of Fe(III) polymerization can form (van Genuchten et al., 2014a; Senn et al., 2015). In aqueous solutions with $(P/Fe)_{init} < (P/Fe)_{crit}$, on the other hand, the initial formation of (Ca)FeP leads to the depletion of dissolved PO_4. In SiO_4-free solutions, continuing Fe(II) oxidation results in the transformation of initially formed (Ca)FeP into Fh and the precipitation of Lp, with complete (Ca)FeP transformation into Fh at $(P/Fe)_{init}$ less than ~0.20 (Voegelin et al., 2013; Senn et al., 2015). In SiO_4-containing solutions, on the other hand, continuing Fe(II) oxidation results in the formation of Fh (Senn et al., 2015). These sequential precipitation processes are reflected in the nanoscale structural heterogeneity of the resulting Fe(III)-precipitates (Voegelin et al., 2013; Senn et al., 2015).

Over time, fresh Fe(III)-precipitates can transform into solids with higher thermodynamic stability and structural order (Gerke, 1993; Cornell and Schwertmann, 2003; Senn et al., 2017). These processes depend on the type of Fe(III)-precipitate, solution pH, temperature, and the concentrations of interfering ions, especially oxyanions that strongly bind to Fe(III) and thereby effectively retard precipitate transformation (Ford, 2002; Violante et al., 2007; Majzlan, 2011; Wang et al., 2015; Hiemstra and Zhao, 2016; Senn et al., 2017; Kraal et al., 2020). The structural transformation of Fe(III)-precipitates typically results in a decrease in sorption capacity and a release of initially co-precipitated oxyanions (Fuller et al., 1993; Mayer and Jarrell, 2000; Senn et al., 2015; Baken et al., 2016; Senn et al., 2017). At near-neutral to alkaline pH, (Ca)FeP can transform into Fh or Lp (McLaughlin and Syers, 1978; Mayer and Jarrell, 2000; Senn et al., 2017). Fh can transform into Lp or goethite (Goe), and also Lp can further transform into Goe (Cornell and Schwertmann, 2003; Senn et al., 2017). To date, however, studies on Fe (III)-mineral transformations have often been conducted under conditions that differ from the conditions in natural waters, and time-resolved aging experiments in synthetic solutions mimicking natural waters are still scarce.

The outgassing of CO_2 from exfiltrating groundwater and the associated increase in pH may promote Fe(III) polymerization and PO_4 release (Griffioen, 2006; Senn et al., 2017), but also leads to an increase of the saturation indices of Ca-carbonates and Ca-phosphates. The release of PO_4 from transforming Fe(III)-precipitates may thus be counteracted by the co-precipitation of PO_4 with Ca-carbonate or the formation of Ca-phosphate (House and Donaldson, 1986; Kleiner, 1988; House, 1990; Valsami-Jones, 2001; House, 2003; Sø et al., 2011; Wright et al., 2011; Bingham et al., 2020). Although the co-precipitation of PO_4 with Ca-carbonate and the precipitation of Ca-phosphate have previously been studied with respect to the fate of PO_4 in natural waters, the coupling between Fe(III)-precipitate formation and aging in water and the formation of Ca-carbonate and Ca-phosphate solids upon CO_2 outgassing, and the impact of these coupled processes on the long-term sequestration of PO_4, have not been studied to date.

We previously determined the interdependent effects of PO_4, Mg, Ca and SiO_4 on the structure and PO_4 uptake of fresh Fe oxidation products formed in aqueous solutions mimicking natural waters in a multifactorial experiment (Senn et al., 2015) and, in a second study, examined how aging of the fresh Fe(III)-precipitates for 30 days at 40 °C affected their structure and PO_4 retention (Senn et al., 2017). The results showed that precipitate transformations during aging can lead to the release of PO_4, its extent depending on the influence of interfering solutes. Insights into the kinetics and mechanisms of Fe(III)-precipitate transformation over time and concomitant Ca-precipitate formation processes were constrained, however, by the lack of time-resolved data on changes in precipitate structure and dissolved PO_4 concentrations.

In the current study, we aimed to follow the transformation of Fe oxidation products in aqueous solutions and consequences for PO_4 retention over up to 100 d of aging with temporal resolution. At a total Fe concentration of 0.5 mM and two molar $(P/Fe)_{init}$ ratios of 0.30 and 0.05 that result in structurally heterogeneous Fe oxidation products, we examined the interdependent effects of varying concentrations of Mg or Ca and of the presence of SiO_4 on the transformation of the fresh Fe(III)-precipitates over time. In Ca-containing electrolytes, we further assessed the coupled formation of Ca-carbonates and Ca-phosphates and their role in longer-term PO_4 retention. The characterization of fresh and aged solids included the quantification of different Fe(III)-precipitate fractions, the description of the nanoscale morphology, and the quantification of the elemental composition of the solids. This detailed structural information was complemented with data on changes in dissolved PO_4 concentrations to unravel the interplay and timescales of different solid formation and transformation processes and their importance for PO_4 retention over time.

2. Materials and methods

2.1. Formation and aging of Fe(III)- and Ca-precipitates

Laboratory experiments on the formation and aging of Fe(III)- and Ca-precipitates were performed following a similar protocol as in earlier work (Senn et al., 2015, 2017; Senn et al., 2018). As further detailed below, the experiments were conducted in bicarbonate-buffered solutions at a total Fe concentration of 0.5 mM at two initial molar PO_4/Fe ratios ($(P/Fe)_{init}$) of 0.30 and 0.05 in ten different background electrolytes (Na, lowMg, midMg, Mg, lowCa, midCa, Ca, Na + Si, Mg + Si, Ca + Si) that varied with respect to the concentrations of the background electrolyte cations Na, Mg and Ca and the absence or presence of SiO_4 (at $(Si/Fe)_{init}$ of 1.0). The experiments were started by adding 0.5 mM dissolved Fe(II) to the aerated solutions adjusted to pH 7.0. After 4 h

when Fe oxidation was expected to be complete, the pH was raised to 7.9 by aeration. Subsequently, the suspension were allowed to age for up to 100 days at 25 °C. Solutions and solids were regularly sampled over the course of the experiments. The experimental conditions are summarized in the supplementary material (SM) in Table S1. All chemicals were reagent grade from Merck or Sigma Aldrich.

Background electrolytes were prepared as follows: Na electrolyte by dissolving 8 mM $NaHCO_3$ in doubly-deionized (DDI) water (18.2 M Ω cm, Milli-Q® Element, Millipore) purged with CO_2 gas; Mg electrolyte was prepared by dissolving 4 mM MgO overnight in DDI water purged with CO_2 gas (purging time ~15 min) in a closed Schott flask to prevent degassing; Ca electrolyte by dissolving 4 mM $CaCO_3$ identically overnight in DDI water purged with CO_2 gas, resulting in clear solutions with a pH of 5.5–5.6. The electrolytes Na + Si, Mg + Si and Ca + Si containing SiO_4 were prepared by spiking 0.5 mM SiO_4 from an alkaline stock solution (100 mM $Na_2SiO_3{\cdot}9H_2O$, prepared daily) to the acidic Na, Ca, or Mg background electrolytes. After the dissolution of Na, Mg, Ca and SiO_4 (where used), the pH of the electrolytes was raised to 7.0 (±0.1) by bubbling with pressurized air. Calculations using the PHREEQC software with the MinteqA2 V4 database (Parkhurst and Appelo, 1999) indicated that the adjustment to pH 7.0 resulted in solutions with a dissolved inorganic carbon (DIC) concentration of ~9.6 mM, in equilibrium with a CO_2 partial pressure of ~47 mbar (without $CaCO_3$ precipitation in the Ca-containing electrolytes).

Subsequently, 2 µM of arsenate (AsO_4), (4 mM $Na_2HAsO_4{\cdot}7H_2O$; neutral stock solution) and 2 µM of cadmium (Cd) (4 mM CdCl; acidic stock solution) were added to each electrolyte at pH 7.0. These trace elements were added to study their binding and retention by Fe(III)- and Ca-precipitates, but also to gain complementary insights into phase formation and transformation processes by interpreting AsO_4 sequestration in comparison to PO_4 and Cd sequestration in comparison to Mg and Ca (results to be published separately).

From the Na (8 mM Na), Mg (4 mM Mg) and Ca (4 mM Ca) electrolytes, the electrolytes lowMg (0.4 mM Mg, 7.2 mM Na), midMg (1.2 mM Mg, 5.6 mM Na), lowCa (0.4 mM Ca, 7.2 mM Na) and midCa (1.2 mM Ca, 5.6 mM Na) were prepared by mixing Na, Mg and/or Ca electrolytes in the required volume ratios. In the following sections, the samples are referred as the electrolyte and molar $(P/Fe)_{init}$ (e.g. Na 0.30/0.05, Mg 0.30/0.05, Ca 0.30/0.05, midMg 0.30/0.05, midCa 0.30/0.05, lowMg 0.30/0.05, lowCa 0.30/0.05, Na + Si 0.30/0.05, Mg + Si 0.30/0.05, Ca + Si 0.30/0.05).

For the synthesis and aging of Fe(III)- and Ca-precipitates, 3 L of the pH-adjusted background electrolytes were transferred into polypropylene (PP) bottles. PO_4 was then spiked to the electrolytes using a neutral stock solution (50 mM $NaH_2PO_4{\cdot}H_2O$) at levels of 0.15 mM and 0.025 mM to achieve initial molar P/Fe ratios ($(P/Fe)_{init}$) of 0.30 and 0.05, respectively. To initiate the oxidation and precipitation of Fe, 0.5 mM Fe(II) were spiked to the background electrolytes (50 mM $FeSO_4{\cdot}7H_2O$, 1.0 mM HCl, acidic stock; prepared daily). Immediately upon Fe addition, the solutions were intensely agitated to ensure rapid mixing, and unfiltered suspension aliquots were collected (10 mL, acidified to 0.65% (v/v) HNO_3) for the analysis of total elemental concentrations of Fe, P, Si, Na, Ca, and Mg (and As, Cd) by inductively-coupled plasma – mass spectrometry (ICP-MS, Agilent 8900). The total element concentrations are shown in Tables S2 and S3. The bottles were then closed and left in dark for a period of 4 h at 25 °C, after which Fe(II) oxidation was deemed complete (>99%). A filtered aliquot was then collected from each suspension (10 mL, 0.2 µm nylon filters, Whatman; acidified to 0.65% (v/v) HNO_3) for the analysis of dissolved element concentrations by ICP-MS. The precipitated solids were collected by filtering 300 mL of suspension through cellulose nitrate filters (Whatman; 0.1 µm; 47 mm diameter). The precipitates on filter membranes were washed by passing 50 mL of DDI water and subsequently dried under a stream of pressurized dry air. The dried solids were stored in a desiccator for later analysis by X-ray absorption spectroscopy (XAS), X-ray diffraction (XRD), and Fourier-transform infrared spectroscopy (FTIR) and for acid digestion. Sample preparation for precipitate analysis by scanning transmission electron microscopy (STEM) was performed on a laminar flow-bench to prevent sample contamination from room air. First, 20 µL of precipitate suspension were pipetted onto a transmission electron microscopy (TEM) grid (Cu, holey carbon), and drawn through the grid using a filter paper. The grids were washed by drawing 40 µL of DDI water through them, and were stored in a grid box in a desiccator cabinet for later analysis by STEM.

After the first sampling of the solutions and the fresh solids, the pH of the suspensions was raised from 7.0 to 7.9 by purging with pressurized air (flow rate: 160 mL/min, time 12–15 min). Calculations using PHREEQC (assuming no $CaCO_3$ precipitation in Ca-containing electrolytes) indicated that this procedure reduced the DIC concentrations of the suspensions to ~7.1 mM, in equilibrium with a CO_2 partial pressure of ~5 mbar. After pH 7.9 was reached, the suspensions were left to age at constant 25 °C in the dark up to 100 days with regular pH monitoring and sampling of solids and solutions by filtration of suspensions as described for the initial sampling. In the 4 mM Ca electrolytes at both $(P/Fe)_{init}$ 0.30 and 0.05 and with/without SiO_4 (Ca 0.30, Ca + Si 0.30, Ca 0.05, Ca + Si 0.05), white precipitates started to form onto the bottle walls during the aging period. After the last sampling (100 d) was completed and all remaining solution had been removed, these precipitates were scrapped from the bottle walls using a steel spatula (yields were ~1 mg for Ca 0.30; ~5–10 mg for other electrolytes). The white wall precipitates were dried under a stream of pressurized air for analysis by FTIR.

To directly quantify the elemental composition of selected solids, solids from four time points from each treatment (electrolyte and $(P/Fe)_{init}$ level) were acid digested in duplicates. Either 1.50 (±0.20) or 2.00 (±0.20) mg of solid were exactly weighed into 15-mL PE tubes and dissolved in 10 mL of ~0.1 M HCl (1% (v/v) of 32% HCl) overnight on a tabletop shaker (300 rpm). The extracts were then diluted for analysis by ICP-MS.

2.2. ICP-MS analyses

Unfiltered and filtered acidified samples were diluted with 1.0% HNO_3 solution for the analysis of Fe, P, Si, Ca, Mg, Na and other elements by Agilent 8900 triple-quadrupole ICP-MS (Agilent Technologies, Tokyo, Japan). Phosphorus was measured by oxygen mass shift mode as PO^+ (m/z 47). Silicon was measured by hydrogen on-mass mode. From the concentrations of Fe, P, Si, Ca, and Mg in the initial unfiltered suspensions and the concentrations in filtered suspensions, the concentrations in suspended solids and the resulting element ratios, e.g. the molar precipitate P/Fe ratio $(P/Fe)_{ppt}$, were calculated. The concentrations of P in 0.2 µm filtered samples were assumed to correspond to dissolved PO_4.

2.3. X-ray diffraction (XRD) analysis

For X-ray diffraction (XRD) measurements, 10 (±1) mg of sample were suspended in ethanol, deposited onto a low-background Si-slide, and allowed to dry. XRD patterns were recorded from 10° to 90° 2θ with a step size of 0.017° and a measurement time of 2.5 h or 7 h per sample using Co Kα radiation (X'Pert Powder diffractometer with X'Celerator detector, PANalytical, Malvern, the Netherlands). The diffractograms were evaluated by using HighScore + software (Malvern PANalytical) for baseline determination and peak profile analysis. The full-width at the half maxima (FWHM) of the diffraction peaks of lepidocrocite at 15.97° 2θ ((hkl); d_{hkl} 6.26 Å) and 31.20° ((hkl); d_{hkl} 3.29 Å), and calcite at 34.30° 2θ ((hkl); d_{hkl} 3.02 Å) were determined for calculation of coherently scattering domain (CSD) sizes using the Scherrer equation.

2.4. Fourier-transform infrared spectroscopy (FTIR)

The samples were measured with Fourier-transform infrared

spectroscopy (FTIR) on a Biorad FTS 575 C instrument with a liquid N_2 cooled MCT detector and an attenuated total reflectance (ATR) unit (Harrick Meridian diamond single reflection Split Pea ATR unit; 20 KHz speed with 5 KHz filter). Measurement range for the spectra was 400–4500 cm^{-1}. For baseline correction, a linear function (straight line) was fit through the data in the two wavenumber regions 1800–1850 cm^{-1} and 2400–2450 cm^{-1} (where no absorbance was expected) and subtracted from the spectra. For a semi-quantitative assessment of the spectral contributions of sorbed PO_4, SiO_4, and HCO_3, and of Lp relative to total Fe(III) in the precipitates, the baseline-corrected spectra were scaled to an average absorbance of 0.35 in the wavenumber region 455–460 cm^{-1}. This range is dominated by Fe–O vibrations present in all Fe(III)-precipitates formed in these experiments. Baseline subtraction and scaling were performed with Octave (GNU). No corrections were applied to spectra containing substantial signal contributions from calcite or Ca-phosphate.

2.5. Fe K-edge extended X-ray absorption fine structure (EXAFS) spectroscopy

For the analysis of the solids by Fe K-edge extended X-ray absorption fine structure (EXAFS) spectroscopy, about 1.5 mg of the air-dried precipitates (~1.0 mg Fe) were thoroughly mixed with ~50 mg of cellulose and pressed into 7 mm diameter pellets (to achieve an absorption edge step of ~0.5–1.0). The spectra were recorded at the SUL-X and the XAS beamlines at the KIT Light Source (Karlsruhe Institute of Technology; Germany) and at the SuperXAS beamline at the Swiss Light Source (SLS, Paul Scherrer Institute, Villigen, Switzerland). For the extraction of the EXAFS spectra and their evaluation by linear combination fitting (LCF), the software code Athena was used (Ravel and Newville, 2005). A first order polynomial was fit to the pre-edge (−100 to −30 eV before the edge) for background removal, and a second order polynomial was fit to the post-edge (50–400 eV) for normalization (edge step calculated at 7128.5 eV). The EXAFS spectra were extracted by using the Autobk algorithm (R_{bkg} = 0.9; *k*-weight = 3; spline *k*-range 0–11.8 $Å^{-1}$). The Fourier-transformed EXAFS spectra were calculated over the k-range 2.5–10.5 $Å^{-1}$ using a Kaiser-Bessel window (with dk = 2 $Å^{-1}$). The sample spectra were analyzed by linear combination fitting (LCF) over the k-range 2–11 $Å^{-1}$ using suitable endmember spectra, similar to previous work (Senn et al., 2015). Individual fractions were constrained to values between 0 and 1, but the sum of the fractions was not constrained.

2.6. Scanning transmission electron microscopy (STEM)

The morphology of the precipitates were characterized using a secondary electron (SE) and a high-angle annular dark field (HAADF) detector of a scanning transmission electron microscope (STEM, HD2700Cs, Hitachi, Japan). For image analysis, the software suite DigitalMicrograph (V.1.82, Gatan Inc., CA, USA) was used. Elemental distribution maps of individual precipitates were recorded using an energy dispersive X-ray (EDX) analysis system coupled to a STEM (Talos F200X, Super-X EDS, 4 detector configuration, ThermoFischer Scientific, USA). For data evaluation, the software code Velox (V. 3.0.0.815, ThermoFischer Scientific, USA) was used. Details on the data analysis are given in the SM Section S7.2.

2.7. Calculation of saturation indices of Ca-phosphates and calcite

For the Ca-containing treatments, the saturation indices (SI) of Ca-phosphates and calcite were calculated based on the measured pH and dissolved Na, Ca and PO_4 concentrations. The concentration of bicarbonate was calculated from the measured concentrations of Na and Ca, assuming bicarbonate to be the main charge-balancing anion. The Davies equation was used for the calculation of the activity coefficients of mono-, di- and trivalent ions, based on the ionic strength estimated from the nominal concentrations of Na and Ca and of bicarbonate as charge-balancing anion. Further details on the calculations and the solubility products used are provided in the SM Section S8.

2.8. Kinetic modelling of Fe(III)-precipitate transformations and molar $(P/Fe)_{ppt}$

A kinetic model was set up to describe the changes in Fe(III)-precipitate structure and composition over time, i.e., the changes in EXAFS LCF-derived Fe(III)-precipitate fractions and in the $(P/Fe)_{ppt}$ of the solids (as calculated from residual dissolved element concentrations). Fit parameters were: (i) The initial fractions of (Ca)FeP, Fh and Lp after the 4-h oxidation period), (ii) first-order rate coefficients for (Ca)FeP transformation into Lp, (Ca)FeP transformation into Fh, and Fh transformation into Lp, and (iii) the molar P/Fe ratios of (Ca)FeP Fh and Lp in each treatment. Further details on the model setup and on fit results are provided in the results Section 3.4.3 and the SM section S6.

3. Results

3.1. Temporal changes in dissolved element concentrations, pH, and precipitate composition

3.1.1. Dissolved phosphate concentrations

The absolute and relative dissolved concentrations of PO_4 after Fe(II) oxidation and after 100-d aging period at both $(P/Fe)_{init}$ 0.30 and 0.05 are shown in Table 1. The dissolved PO_4 concentrations after Fe(II) oxidation reflected the effective removal of PO_4 by co-precipitation with the fresh Fe precipitates. At both $(P/Fe)_{init}$, the highest residual dissolved PO_4 fractions were observed in the Na electrolyte. Increasing levels of Mg and especially Ca, and the presence of SiO_4 all led to lower dissolved PO_4 fractions. Higher dissolved fractions were in general observed at $(P/Fe)_{init}$ of 0.05 than at 0.30, but still corresponded to lower absolute PO_4 concentrations. Changes in dissolved PO_4 fractions in the suspensions over the course of the 100-d aging period are shown in Fig. 1. Over time, PO_4 was released back into the solutions, pointing to precipitate transformations during aging. The extent of PO_4 release depended on the type and concentration of the electrolyte cation, the $(P/Fe)_{init}$, and whether the solution contained SiO_4 or not.

At $(P/Fe)_{init}$ of 0.30, the release of PO_4 was highest in the Na electrolyte where it reached a plateau at ~77% of the total PO_4 after 25–50 days (Fig. 1a). The PO_4 release decreased with increasing Mg concentration from the Na 0.30 to the Mg 0.30 treatment (Fig. 1a). An even larger effect than for Mg was observed for increasing levels of Ca from the Na 0.30 to the Ca 0.30 treatment (Fig. 1c). In the Ca 0.30 treatment, the fraction of dissolved PO_4 started to decrease again after ~50 days of aging, pointing to specific interactions of PO_4 with Ca. Comparison of the SiO_4-containing electrolytes (Fig. 1e) with the corresponding SiO_4-free electrolytes (Fig. 1ac) showed that SiO_4 inhibited PO_4 release in the presence of all cations.

At $(P/Fe)_{init}$ of 0.05 (0.025 mM PO_4), the trends in the extent of PO_4 release over time as a function of Mg or Ca concentration and absence/presence of SiO_4 roughly corresponded to the trends observed at $(P/Fe)_{init}$ 0.30 (Fig. 1). However, the release of PO_4 mostly occurred within

Table 1
Dissolved PO_4 in precipitate suspensions after Fe(II) oxidation and after aging of the suspensions for 100 d; expressed as absolute concentrations and as percentages of total PO_4.

Electrolyte	After Fe(II) oxidation				After 100 d aging			
	$(P/Fe)_{init}$ 0.30		$(P/Fe)_{init}$ 0.05		$(P/Fe)_{init}$ 0.30		$(P/Fe)_{init}$ 0.05	
	(μM)	(%tot)	(μM)	(%tot)	(μM)	(%tot)	(μM)	(%tot)
Na	6.0	4.0%	3.5	14%	110	77%	15	62%
lowMg	3.2	2.1%	2.7	11%	95	63%	11	44%
midMg	3.2	2.1%	2.2	8.8%	81	54%	9.6	38%
Mg	2.5	1.7%	1.7	6.9%	74	49%	8.9	36%
lowCa	3.5	2.3%	2.5	10%	98	65%	11	46%
midCa	2.5	1.6%	1.9	7.5%	74	50%	5.2	21%
Ca	1.6	1.0%	1.4	5.5%	20	13%	0.8	3.1%
Na + Si	0.3	0.2%	<0.1	<0.4%	42	28%	0.9	3.5%
Mg + Si	0.3	0.2%	<0.1	<0.4%	21	14%	0.2	0.9%
Ca + Si	0.2	0.1%	<0.1	<0.4%	5.9	3.9%	0.3	1.0%

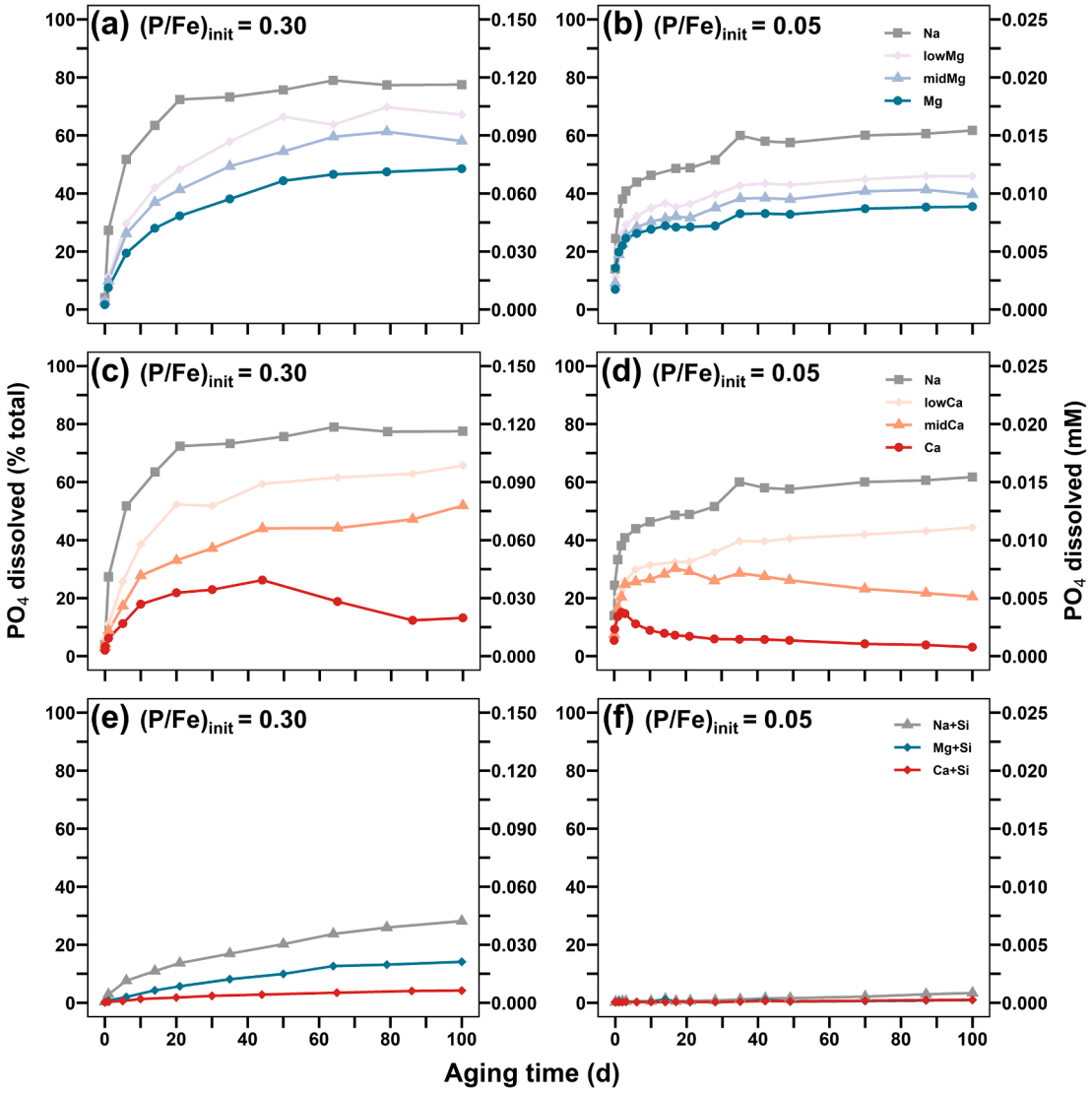

Fig. 1. Dissolved phosphate in precipitate suspensions during aging for up to 100 days. (a, c, e) Molar $(P/Fe)_{init}$ of 0.30 (0.15 mM P_{tot}), (b, d, f) Molar $(P/Fe)_{init}$ of 0.05 (0.025 mM P_{tot}).

the first 10 days of aging, and the final released fractions tended to be lower than at $(P/Fe)_{init}$ of 0.30, especially in the SiO_4-containing electrolytes. In the Ca 0.05 and midCa 0.05 treatments, the fraction of dissolved PO_4 initially increased but started to decrease again after ~3 and ~20 days, respectively, pointing to specific Ca-PO_4 interactions (Fig. 1d).

3.1.2. Changes in suspension pH and dissolved Ca

Over the 100-d aging period, the pH of the Ca-free precipitate suspensions in general increased from pH 7.9 to pH 8.3 ± 0.3 at a $(P/Fe)_{init}$ of 0.30 and to pH 8.5 ± 0.2 at $(P/Fe)_{init}$ of 0.05 (Fig. S1), due to continuing CO_2 outgassing and equilibration at ambient CO_2 partial pressure. A wider range of trends in suspension pH was observed in the Ca-containing suspensions (Fig. 2), where over time the pH either (i) increased to a similar extent as in the Ca-free treatments (lowCa 0.05, lowCa 0.30, midCa 0.30), (ii) increased less (Ca 0.30, Ca + Si 0.30), (iii) remained nearly constant (midCa 0.05, Ca 0.05) or (iv) even decreased (Ca + Si 0.05), pointing to differences in Ca-carbonate precipitation during aging. The fractions of dissolved Ca and the suspension pH for the Ca-containing electrolytes are shown in Fig. 2. In the Ca and midCa electrolytes at $(P/Fe)_{init}$ of 0.05, dissolved PO_4 started to decrease after 3 and 20 d (Fig. 1b), in parallel to the decrease in dissolved Ca and related changes in pH (Fig. 2), suggesting that PO_4 was co-precipitated with Ca-carbonate. In the Ca 0.30 treatment, on the other hand, dissolved PO_4 during aging rapidly increased to above 20 μM, a level known to inhibit the formation of Ca-carbonate (House, 1987; Plant and House, 2002). Accordingly, the decrease in dissolved PO_4 in the Ca 0.30 treatment after 50 d of aging was tentatively attributed to Ca-phosphate precipitation. Saturation indices for calcite and different Ca-phosphates were calculated for the Ca-containing treatments for each sampling time (Tables S11 and S12). The calculations indicated that calcite was oversaturated in all Ca-containing electrolytes after raising the pH to 7.9. Supersaturation of Ca-phosphates other than hydroxyapatite, on the other hand, was only reached at the higher $(P/Fe)_{init}$ of 0.30.

3.1.3. Molar element ratios in precipitates calculated from dissolved concentrations and acid digestion

From the total and dissolved concentrations of P, Si, and Fe, the molar PO_4/Fe and SiO_4/Fe ratios in the precipitates ($(P/Fe)_{ppt}$, $(Si/Fe)_{ppt}$) were calculated for all treatments (Tables S4 and S5). In addition, the molar element ratios of selected precipitates were also determined by acid digestion (Tables S4 and S5). For selected treatments, $(P/Fe)_{ppt}$ ratios derived from solution data and acid digestion are listed in Table 2. In general, molar PO_4/Fe ratios determined from the solution data and by acid digestion were in reasonable agreement. Notable exceptions were observed for some aged samples from Ca-containing electrolytes, where the acid digest returned markedly lower $(P/Fe)_{ppt}$ than calculated from the solution data: Ca 0.30 100 d, Ca 0.05 21 d and 70 d, and midCa 0.05 21 d and 70 d. Considering that some PO_4 in these treatments was presumably removed by uptake into Ca-phosphate or Ca-carbonate during aging, the discrepancy suggested that these Ca-precipitates preferentially accumulated on the walls of the reaction containers, as observed previously (Senn et al., 2015, 2017). Consequently, the $(P/Fe)_{ppt}$ from acid digestion was supposed to more closely reflect the $(P/Fe)_{ppt}$ of the Fe(III)-precipitates in the suspensions.

3.2. X-ray diffraction analysis

The XRD patterns of fresh and up to 100 days aged precipitates formed in the Na, Ca, and Ca + Si electrolytes at $(P/Fe)_{init}$ of 0.30 and

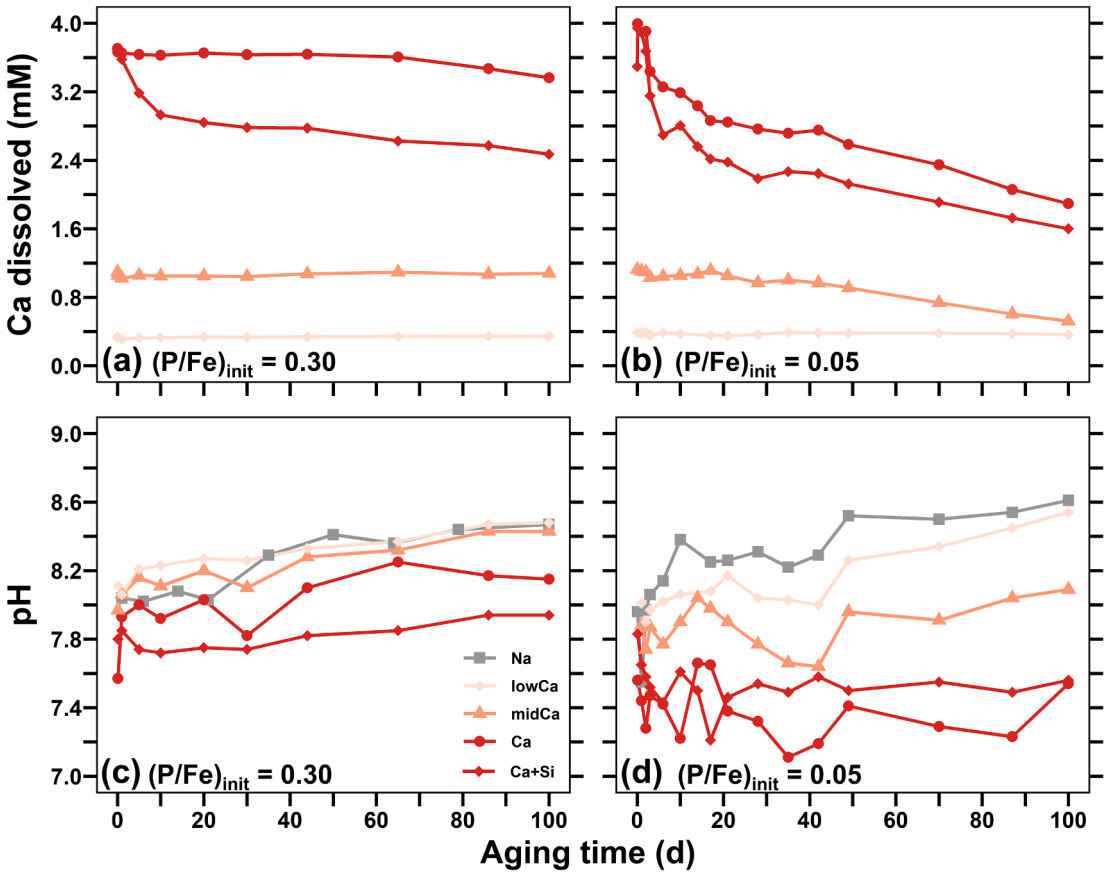

Fig. 2. Dissolved fraction of Ca (a, b) and pH (c, d) over the 100-d aging period in Ca-containing electrolytes. Data for $(P/Fe)_{init}$ of 0.30 in (a,c) and for $(P/Fe)_{init}$ of 0.05 in (b, d). In (c, d), the pH from the corresponding Na treatments is plotted for comparison.

Table 2
Comparison of $(P/Fe)_{ppt}$ ratios of selected precipitates as derived from solution data, acid digestion, and STEM-EDX (entire mapped sample area).

	$(P/Fe)_{init}$ 0.30				$(P/Fe)_{init}$ 0.05			
Electrolyte	**Aging time (d)**	**Solution $(P/Fe)_{ppt}$**	**Acid digestion $(P/Fe)_{ppt}$**	**STEM-EDX (bulk) $(P/Fe)_{ppt}$**	**Aging time (d)**	**Solution $(P/Fe)_{ppt}$**	**Acid digestion $(P/Fe)_{ppt}$**	**STEM-EDX (bulk) $(P/Fe)_{ppt}$**
Na	0	0.29	0.28	0.28	0	0.04	–	0.06
	35	0.08	0.08	–	1	0.03	0.03	–
	49	0.08	–	0.08	70	0.02	0.02	–
	100	0.07	0.05	0.05	100	0.02	–	0.03
Mg	0	0.29	0.29	0.28	0	0.05	–	0.06
	35	0.18	0.17	–	1	0.04	0.04	–
	49	0.16	–	–	70	0.03	0.03	–
	100	0.16	0.13	0.14	100	0.03	–	0.03
Ca	0	0.31	0.30	0.29	0	0.05	–	0.06
	35	0.25	0.22	–	1	0.04	0.04	–
	49	0.25	0.23	0.30	70	0.05	0.03	–
	100	0.27	0.16	0.21	100	0.05	0.05	0.02
Na + Si	0	0.31	0.31	0.26	0	0.05	–	0.06
	35	0.24	0.24	–	1	0.05	0.05	–
	54	0.23	–	0.22	70	0.05	0.04	–
	100	0.23	0.20	0.21	100	0.05	–	0.05
Mg + Si	0	0.31	0.32	0.32	0	0.05	–	0.06
	35	0.28	0.27	–	1	0.05	0.05	–
	54	0.27	–	0.25	70	0.05	0.05	–
	100	0.27	0.25	0.25	100	0.05	–	0.05
Ca + Si	0	0.32	0.33	0.31	0	0.06	–	0.05
	35	0.31	0.30	–	1	0.05	0.05	–
	54	0.31	–	0.30	70	0.05	0.05	–
	100	0.29	0.27	0.28	100	0.05	–	0.04

0.05 are shown in Fig. 3, the complete sets of XRD patterns for all treatments are shown in Figs. S4–S6. The XRD patterns allowed to gain information on the crystalline components in the suspended solids.

3.2.1. *SiO_4-free electrolytes*

With respect to crystalline Fe(III)-solids in the precipitates formed in the absence of SiO_4, the XRD patterns revealed the main peaks of Lp, whose breadth was indicative of small particle size and/or low crystallinity. No goethite peaks were observed in any of the samples over the aging period. The heights of the Lp peaks in samples formed at $(P/Fe)_{init}$ of 0.30 were much lower than of corresponding samples at $(P/Fe)_{init}$ 0.05, at least partly reflecting the formation of a larger share of amorphous Fe(III)-phosphate and/or Fh at higher $(P/Fe)_{init}$ Over the course of precipitate aging, the Lp peak widths decreased in all SiO_4-free treatments, indicative of an increase in Lp crystallite sizes over time. From the FWHMs of the (0 2 0) peak of Lp (15.97° 2θ; Co Kα) formed and aged in the Na, Mg, and Ca electrolytes at $(P/Fe)_{init}$ 0.30 and 0.05, coherently scattering domain (CSD) sizes indicative for the extent of layer stacking were calculated using the Scherrer equation (Table S7). At $(P/Fe)_{init}$ of 0.30, the CSD increased from 1.0 nm to 1.8 nm in the Na electrolyte over 100 d aging, from 0.7 nm to 1.6 nm in the Mg electrolyte, and from 0.8 to 1.7 nm in the Ca electrolyte. At $(P/Fe)_{init}$ 0.05, the CSD increased from 1.6 nm to 2.5 nm in Na electrolyte, from 1.4 nm to 1.8 nm in Mg electrolyte, and from 1.4 nm to 2.0 nm in Ca electrolyte. Considering a layer spacing of roughly 0.6 nm along the unit-cell b-axis, the calculated CSD sizes were indicative of Lp crystallites consisting on average of between 2 (fresh precipitate in Mg 0.30 treatment) to 5 (aged precipitate in Na 0.05 treatment) corrugated Fe layers.

The XRD patterns from the Ca 0.30 and 0.05 treatments indicated the formation of calcite, with an earlier onset and larger extent at $(P/Fe)_{init}$ of 0.05 than 0.30. Some calcite formation was also observed in the midCa 0.05 treatment, whereas no calcite formation was detected in the midCa 0.30, lowCa 0.30 and lowCa 0.05 treatments (Figs. S4 and S5), in line with trends in dissolved Ca and pH (Fig. 2). In the 100-days aged Ca 0.30 precipitate, on the other hand, a broad peak at 36° 2-θ pointed to the precipitation of (amorphous) Ca-phosphate (Dorozhkin, 2010), in line with the decrease in dissolved PO_4 after 50 d of aging (Fig. 1c). Trends in the FWHM of the calcite (104) peak (34.30° 2-θ) indicated that the CSD of the calcite crystals formed at the onset of the experiment decreased with increasing residual dissolved PO_4 and that the CSD slightly increased as further calcite formed during aging.

3.2.2. *SiO_4-containing electrolytes*

For the Si-containing electrolytes, the XRD results confirmed that SiO_4 inhibited the formation of crystalline Fe(III)-precipitates during initial Fe oxidation and subsequent precipitate aging (Fig. 3, Fig. S6). Instead, apart from the peaks of crystalline Ca-precipitates, the respective XRD patterns only revealed a broad peak at 35–40° 2θ (Co Kα) (Fig. 3, Fig. S6). Considering reference peak positions of 38.6° (d-spacing 2.6 Å) for 2-line Fh (Cornell and Schwertmann, 2003) and of 35.5° (d-spacing 3.0 Å) for amorphous Fe(III)-phosphate (Thibault et al., 2009), the peak positions of samples formed at $(P/Fe)_{init}$ of 0.30 and of 0.05 were in line with a higher share of amorphous (Ca-)Fe(III)-phosphate at $(P/Fe)_{init}$ of 0.30 and predominant formation of Fh at $(P/Fe)_{init}$ of 0.05. No significant shifts in these peaks were observed during aging (Fig. 3, Fig. S6).

In analogy to the data from the Ca 0.30 and Ca 0.05 treatments, the XRD patterns of precipitates from the Ca + Si 0.30 and Ca + Si 0.05 treatments pointed to an earlier and larger extent of calcite precipitation at $(P/Fe)_{init}$ of 0.05 than 0.30. For Ca + Si 0.05, the XRD patterns of the 21-d, 49-d, and 100-d aged samples further revealed the formation of a minor share of aragonite that was not observed in any other Ca-containing treatment.

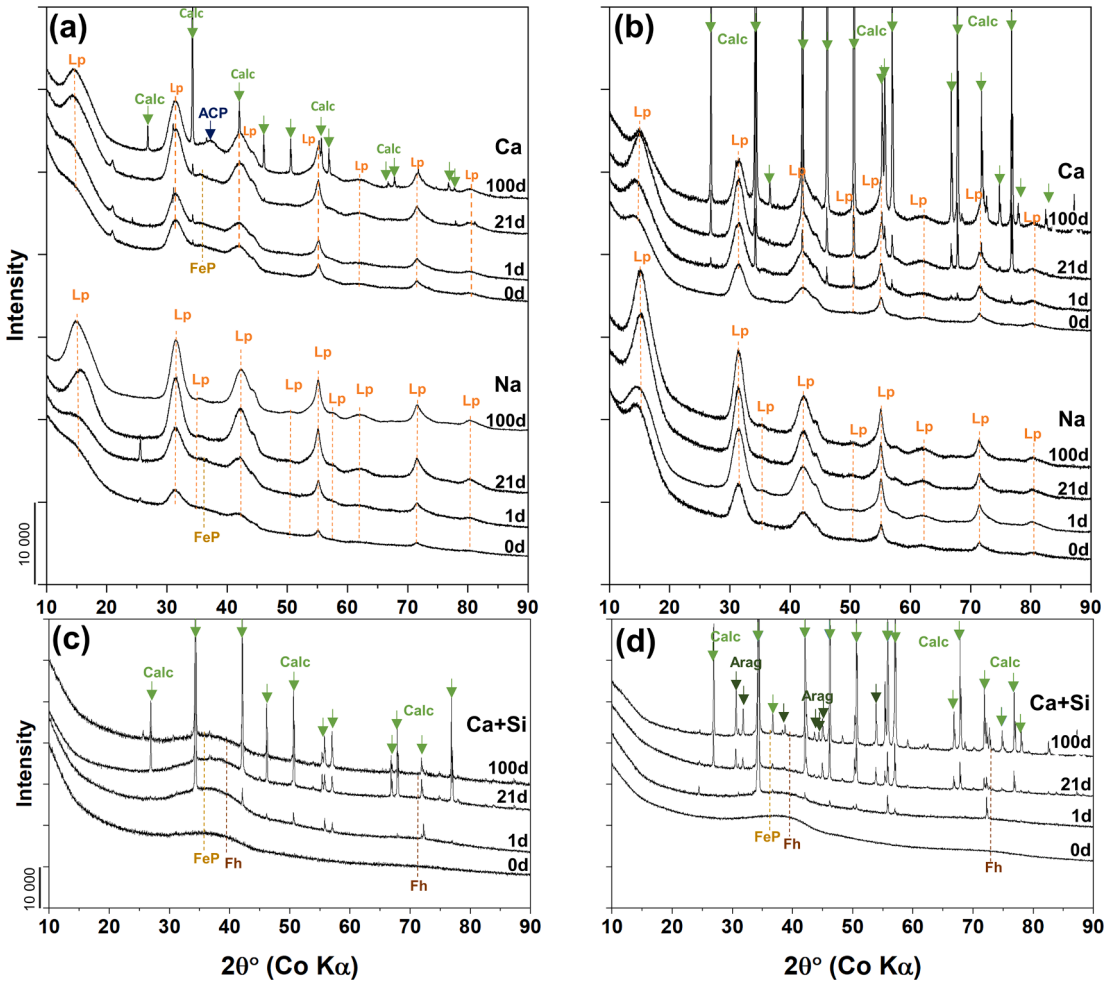

Fig. 3. X-ray diffraction patterns of precipitates formed and aged at $(P/Fe)_{init}$ 0.30 (a, c) and 0.05 (b, d) in Ca, Na, and Ca + Si (c, d) electrolyte. Note: patterns are stacked, and peak heights are also affected by slight variations in sample mass (±10%). Lp: lepidocrocite, FeP: amorphous Fe(III)-phosphate, ACP: amorphous Ca-phosphate, Calc: calcite, Arag: aragonite, Fh: ferrihydrite.

3.3. Fourier transform infrared spectroscopy

The FTIR spectra of fresh and up to 100 d aged precipitates formed in the Na, Ca, and Ca + Si electrolytes at $(P/Fe)_{init}$ of 0.30 and 0.05 are shown in Fig. 4. The complete FTIR results for all treatments are shown in Figs. S8–S9. In addition to the suspended solids, small amounts of Ca-solids collected from the reaction bottle walls after the completion of the aging experiments in Ca and Ca + Si electrolytes were also characterized by FTIR. FTIR probes molecular vibrations arising from Fe- and Ca-precipitates, including structural and adsorbed oxyanions (carbonate, silicate, phosphate), and thus provides insights complementary to the XRD results.

With respect to crystalline Fe(III)-precipitates in the SiO_4-free treatments, the FTIR data confirmed the formation of Lp, which exhibits characteristic peaks at 740 cm^{-1} and 1013 cm^{-1} (wavenumbers) (Cornell and Schwertmann, 2003). The Lp peak at 1013 cm^{-1} was overlain by a broad peak attributed to structural or adsorbed PO_4, composed of several contributions at 973, 1000 and 1081 cm^{-1}, in agreement with ranges reported for PO_4 adsorbed on ferrihydrite (Arai and Sparks, 2001). Over the 100-d aging period, the peak of Lp increased and the peak of PO_4 decreased, in line with the transformation of Fe(III)-phosphate or PO_4-loaded Fh into Lp and the release of PO_4 from the solids. This transformation was most prominent in the Na 0.30 and occurred the least in the Ca 0.05 treatment (Fig. 4), in line with trends in PO_4 release into solution over time (Fig. 1) and XRD results (Fig. 3).

In the spectra of precipitates formed in the SiO_4-containing electrolytes, no Lp peaks were observed (Fig. 4cd), in line with the XRD results (Fig. 3). In agreement with reported spectra of SiO_4 adsorbed onto Fh with broad peaks from 945 to 1009 cm^{-1} (Swedlund et al., 2010), our peaks of solid-bound SiO_4 overlap with the peaks of solid-bound PO_4. Considering the $(P/Fe)_{ppt}$ and $(Si/Fe)_{ppt}$ ratios obtained by acid digestion (Tables S4 and S5), the PO_4 signal dominated the combined peak at $(P/Fe)_{init}$ of 0.30, and the SiO_4 signal at $(P/Fe)_{init}$ of 0.05, but the spectral overlap prevented the interpretation of minor changes in cumulative peak shape during aging.

Peaks of adsorbed carbonate around 1385–1410 cm^{-1} and 1490–1520 cm^{-1} (Villalobos and Leckie, 2001; Bargar et al., 2005) were observed in some of the treatments. The peaks at 1635–1645 are due to various amounts of adsorbed H_2O. In the SiO_4-containing electrolytes, these peaks increased from the Na + Si over the Mg + Si to the Ca + Si electrolyte, and were higher at $(P/Fe)_{init}$ of 0.05 than 0.30, indicating that Ca and to lesser extent Mg promoted carbonate adsorption onto Fh, and that higher levels of PO_4 reduced carbonate uptake through sorption competition (Mendez and Hiemstra, 2018). The increase of the peaks of adsorbed carbonate in the Ca 0.30 treatment during aging, in contrast to the Mg 0.30 or Na 0.30 treatments, might be due to PO_4 uptake by Ca-phosphate, and thus reduced competition of PO_4 with carbonate for sorption onto the Fe(III)-precipitates.

Considering the characteristic peaks of calcite at 1403, 870, and 711 cm^{-1}, the FTIR data confirmed the XRD results with respect to the extent of calcite formation as a function of Ca concentration and $(P/Fe)_{init}$. Furthermore, also FTIR analysis indicated the formation of a minor

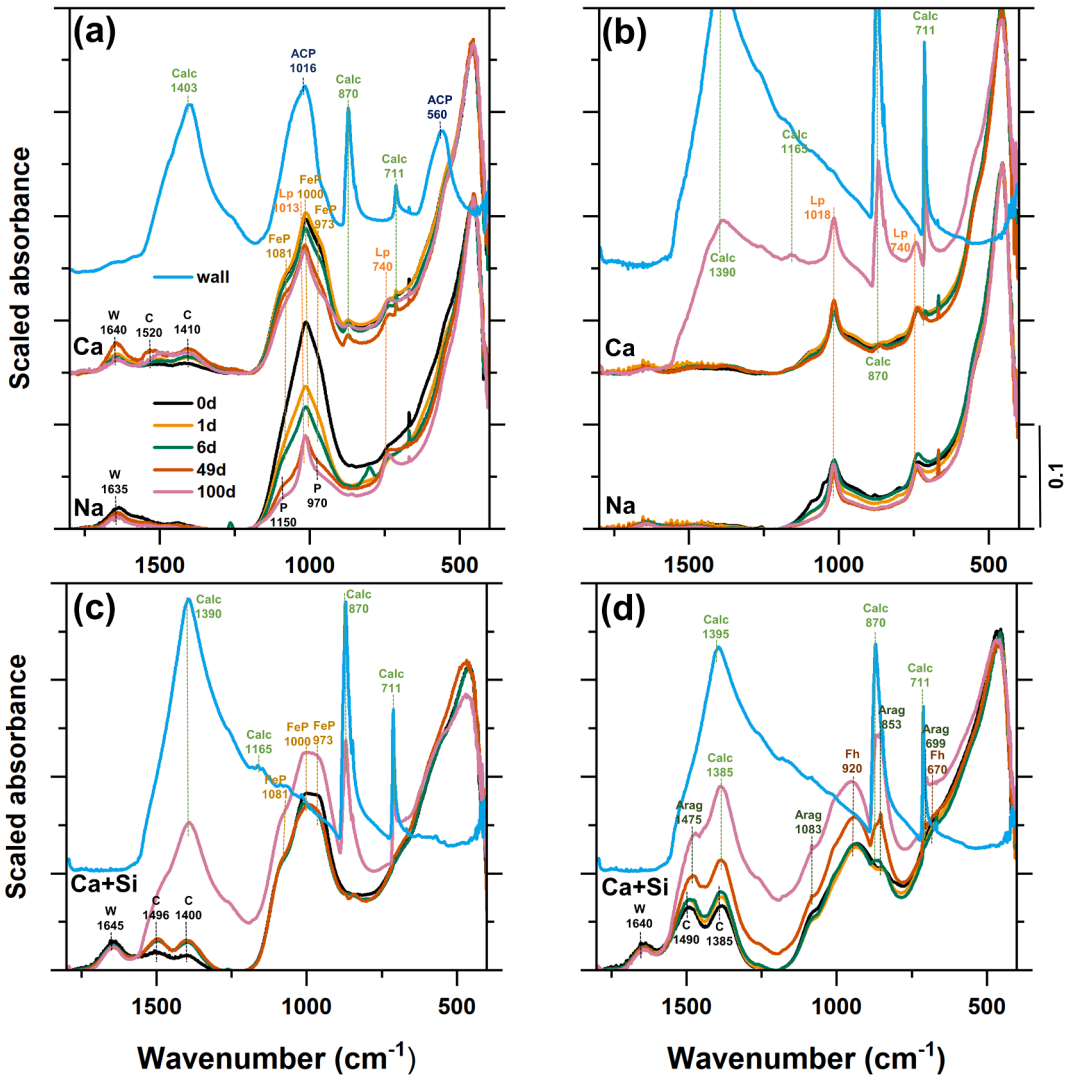

Fig. 4. Fourier-transform IR spectra of precipitates formed and aged at $(P/Fe)_{init}$ 0.30 (a, c) and 0.05 (b, d) in Ca, Na, and Ca + Si (c, d) electrolytes. Lp: lepidocrocite, Fh: ferrihydrite, FeP: amorphous Fe(III)-phosphate, ACP: amorphous Ca-phosphate, Calc: calcite, Arag: aragonite, C: bicarbonate, P: ads. PO_4, w: water.

fraction of aragonite in the Ca + Si 0.05 electrolyte during aging.

Concerning the solids collected from the walls of the reaction bottles after completion of the experiments, the sample from the Ca 0.30 treatment revealed two marked broad peaks at 1016 and 560 cm^{-1}, in good agreement with the reported peaks of amorphous Ca-phosphate (ACP) (Combes and Rey, 2010). This confirmed that Ca-phosphate accumulated on the walls of the reaction container. Additional peaks observed for this sample were characteristic of calcite, which was the only Ca-mineral identified in the wall samples from the Ca + Si 0.30, Ca 0.05 and Ca + Si 0.05 electrolytes (Fig. 4).

3.4. Fe K-edge EXAFS spectroscopy

To quantify the fractions of Fe(III) in amorphous and crystalline Fe (III)-compounds, the fresh and aged precipitates were analyzed by Fe K-edge EXAFS spectroscopy. The Fourier transformed (FT) k^3-weighted EXAFS spectra of selected precipitates in Na, Ca, and Ca + Si electrolytes at $(P/Fe)_{init}$ of 0.30 and 0.05 and reference spectra used for their analysis by LCF are shown in Fig. 5. The k^3-weighted EXAFS spectra of all samples are shown in Figs. S10 and S11.

3.4.1. Reference phases for spectra interpretation and LCF analysis

An initial analysis indicated that the sample spectra could be reproduced with four reference spectra that represent distinct end-member phases with varying extent and mode of FeO_6 octahedra linkage (Senn et al., 2015): (1) Amorphous Fe(III)-phosphate (FeP*) formed by Fe(II) oxidation in bicarbonate-buffered electrolyte with Na or Mg as electrolyte cation. (2) Amorphous Ca-Fe(III)-phosphate (CaFeP*) formed by Fe(II) oxidation in bicarbonate-buffered electrolyte with 4 mM Ca as electrolyte cation. (3) Ferrihydrite (Fh*) formed by Fe(II) oxidation in bicarbonate-buffered electrolyte at $(Si/Fe)_{init}$ of 1.0, containing ~0.1 SiO_4/Fe; here also used as proxy for Fh* formed in the SiO_4-free electrolytes. (4) Poorly-crystalline lepidocrocite (Lp*) formed by Fe(II) oxidation in bicarbonate-buffered electrolyte in the absence of PO_4 and SiO_4. Variations in the extent and mode of FeO_6 octahedra linkage among the different reference materials are mainly reflected in the peak at r (=R + δ(R)) ~ 2.6 Å: The lowest second-shell signal is observed for FeP*, with limited degree of (edge-sharing) linkage of FeO_6 octahedra. The more intense second-shell peak of CaFeP* as compared to FeP* arises from more extensive edge-sharing (albeit still limited) and also some corner-sharing linkage of FeO_6 octahedra (Senn et al., 2015). An even more intense second-shell peak is observed for Fh*, including contributions of edge- and – to lesser extent – corner-sharing linkage of FeO_6 octahedra in ferrihydrite nanocrystals. Notably, the spectrum Fh* also shows an attenuated first-shell Fe–O peak (at r ~ 1.5 Å), reflecting a marked distortion of the FeO_6 octahedra in ferrihydrite and, potentially,

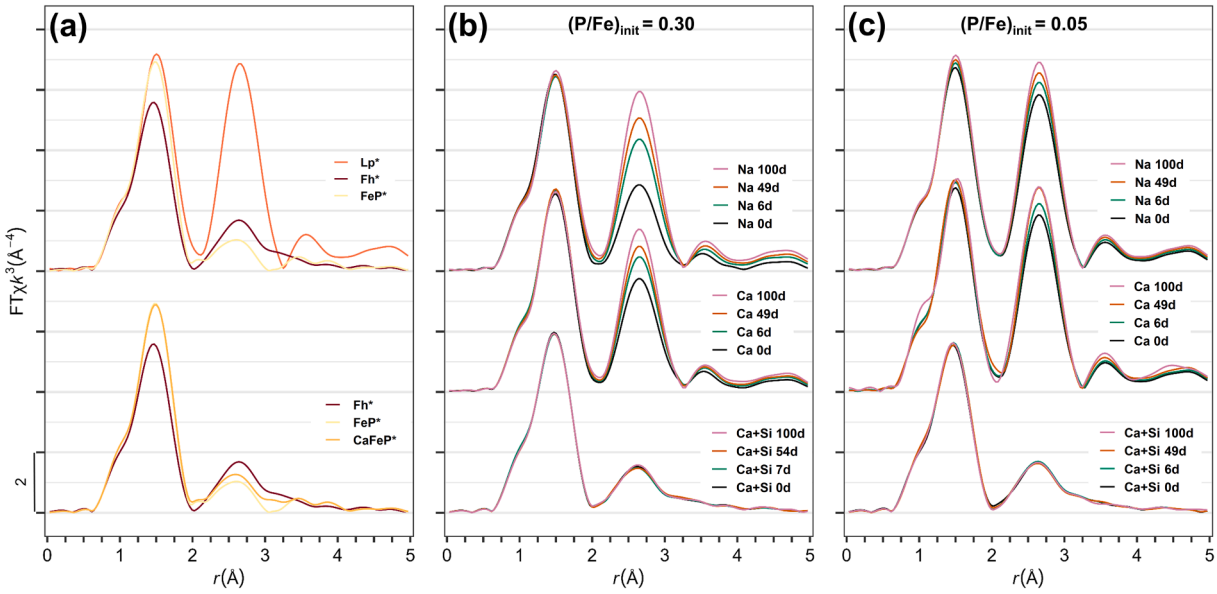

Fig. 5. Fourier-transformed k^3-weighted Fe K-edge EXAFS spectra of (a) reference compounds for LCF analysis, (b) samples formed and aged at $(P/Fe)_{init}$ 0.30 in Na, Ca, and Ca + Si electrolytes, and (c) samples formed and aged at $(P/Fe)_{init}$ 0.05 in Na, Ca, and Ca + Si electrolytes. Reference spectra: Lp*: poorly crystalline lepidocrocite; Fh*: ferrihydrite; FeP* amorphous Fe(III)-phosphate; CaFeP*: amorphous Ca-Fe(III)-phosphate. Note: r corresponds to the sum of the interatomic distance R and the phase shift δ(R).

a minor share of tetrahedrally coordinated Fe(III) (Mikutta, 2011). The largest second-shell signal is observed for Lp*, arising from extensive edge-sharing linkage of FeO_6 octahedra in the corrugated lepidocrocite sheets.

3.4.2. *Spectral trends over time and their quantification by LCF*

Among the SiO_4-free treatments, the largest spectral changes and the largest increase in the second-shell Fe–Fe signal was observed in the Na 0.30 treatment (Fig. 5), in line with the dynamic phase evolution observed by XRD and FTIR. In contrast, the second-shell peak amplitude in the Ca 0.05 treatment was initially much higher, and did not increase as much anymore over time (Fig. 5). In both treatments, the spectral changes could be tentatively attributed to the transformation of CaFeP or Fh into Lp. In the SiO_4-containing treatments Ca + Si 0.30 and Ca + Si 0.05, the spectral signal indicated the formation of CaFeP and Fh and revealed no detectable changes over time (Fig. 5), indicating limited structural transformation of the Fe(III)-precipitates during aging. To quantify the initial Fe(III)-precipitate composition and its changes during aging, the EXAFS spectra were evaluated by LCF using the four reference spectra described above (Fig. 5). The LCF results for samples from all treatments over increasing incubation times are shown in Fig. 6, the reconstructed LCF spectra together with the sample spectra are shown in the SM section S5.

For the SiO_4-free treatments at $(P/Fe)_{init}$ of 0.30, the LCF results indicate the initial formation of mixtures of (Ca)FeP and Lp and a minor fraction of Fh, followed by continuing transformation of (Ca)FeP into Fh and Lp and of Fh into Lp during aging. Both the FeP* and CaFeP* reference spectra were included in the LCF to represent (Ca)FeP in samples formed at $(P/Fe)_{init}$ of 0.30. Despite the similarity of these reference spectra (Fig. 5), and despite the presence of the major spectral contribution of Lp*, LCF in general returned higher shares of CaFeP* and lower shares of FeP* to describe (Ca)FeP in electrolytes with higher Ca concentration, confirming a good sensitivity for even small spectral differences. In the Na 0.30 treatment, the highest initial fraction of FeP was observed. Over time, however, a substantial share of the initially formed FeP was transformed into Lp. In the Ca 0.30 treatment, a higher share of Lp formed during Fe(II) oxidation than in the Na 0.30 treatment, but further transformation of (Ca)FeP into Lp during aging was limited. In the Mg-containing electrolytes, the initially formed fraction of Lp increased with increasing Mg concentration. Remarkably, transformation of FeP during aging led to a marked increase of the fractions of both Lp and Fh (Fig. 6), in contrast to the Na 0.30 and Ca 0.30 treatments, pointing to a distinct effect of Mg. In the SiO_4-containing treatments at $(P/Fe)_{init}$ of 0.30, the initial precipitates were composed of a mixture of (Ca)FeP and Fh. Over time, some transformation of (Ca)FeP into Fh was observed, its extent decreasing along the order Na + Si 0.30 > Mg + Si 0.30 > Ca + Si 0.30.

In the treatments at 0.05 $(P/Fe)_{init}$, the lower PO_4 concentrations allowed for the initial formation of a higher share of Lp (no SiO_4) or Fh (with SiO_4). In the SiO_4-free treatments, only Fh* (but no FeP* and/or CaFeP*) was required to describe the initial non-crystalline precipitate fraction. A limited further increase in the Lp* fraction was observed during aging, indicating the transformation of Fh into Lp. Like at $(P/Fe)_{init}$ of 0.30, increasing levels of Mg led to an increase in the remaining fractions of Fh, in contrast to increasing levels of Ca (Fig. 6). For the SiO_4-containing treatments at $(P/Fe)_{init}$ of 0.05, the LCF results showed that the initial precipitates consisted of a major fraction of Fh and a minor fraction of (Ca)FeP and revealed no detectable changes in Fe speciation during aging.

3.4.3. *Kinetic model of changes in Fe(III)-precipitate fractions and molar (P/Fe) ratios*

The LCF results provided evidence for the transformation of (Ca)FeP into Fh and Lp, and the transformation of Fh into Lp (Fig. 6). In Fig. 7, the LCF fractions (Ca)FeP* (sum of FeP* and CaFeP*), Fh* and Lp* from the treatments Na 0.30, Mg 0.30, Ca 0.30 and CaSi 0.30 are shown as a function of aging time, together with the corresponding $(P/Fe)_{ppt}$ of the bulk precipitates as derived from the solution data (Fig. 1). To quantify the kinetics of the transformations between different Fe(III)-precipitate fractions and to relate changes in the bulk $(P/Fe)_{ppt}$ to changes in precipitate fractions, a simple kinetic model was implemented that accounted for the observed transformation reactions based on first order reaction kinetics,

$$\text{(Ca)FeP} \rightarrow \text{Fh}\ k_{\text{(Ca)FeP-Fh}} \quad (1)$$

$$\text{(Ca)FeP} \rightarrow \text{Lp}\ k_{\text{(Ca)FeP-Lp}} \quad (2)$$

$$\text{Fh} \rightarrow \text{Lp}\ k_{\text{Fh-Lp}} \quad (3)$$

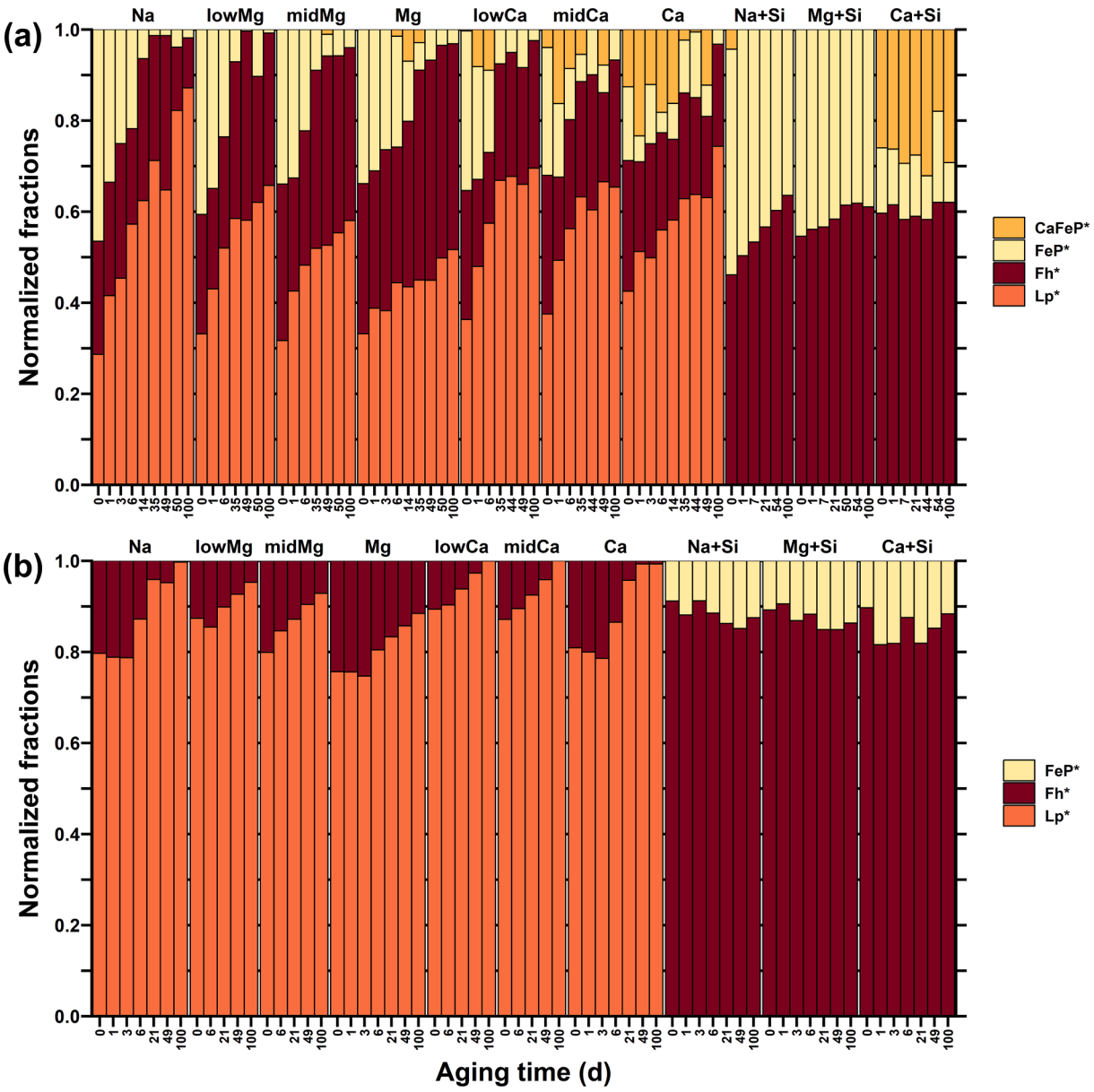

Fig. 6. Results from LCF analysis of the Fe K-edge EXAFS spectra of the precipitates aged up to 100 days at (a) $(P/Fe)_{init}$ 0.30, (b) at $(P/Fe)_{init}$ 0.05. The fit results for the precipitates at $(P/Fe)_{init}$ 0.30 are listed in Table S8 and for the precipitates at $(P/Fe)_{init}$ 0.05 in Table S9. Reference spectra (see Fig. 5): Lp*: poorly crystalline lepidocrocite; Fh*: ferrihydrite; FeP* amorphous Fe(III)-phosphate; CaFeP*: amorphous Ca-Fe(III)-phosphate.

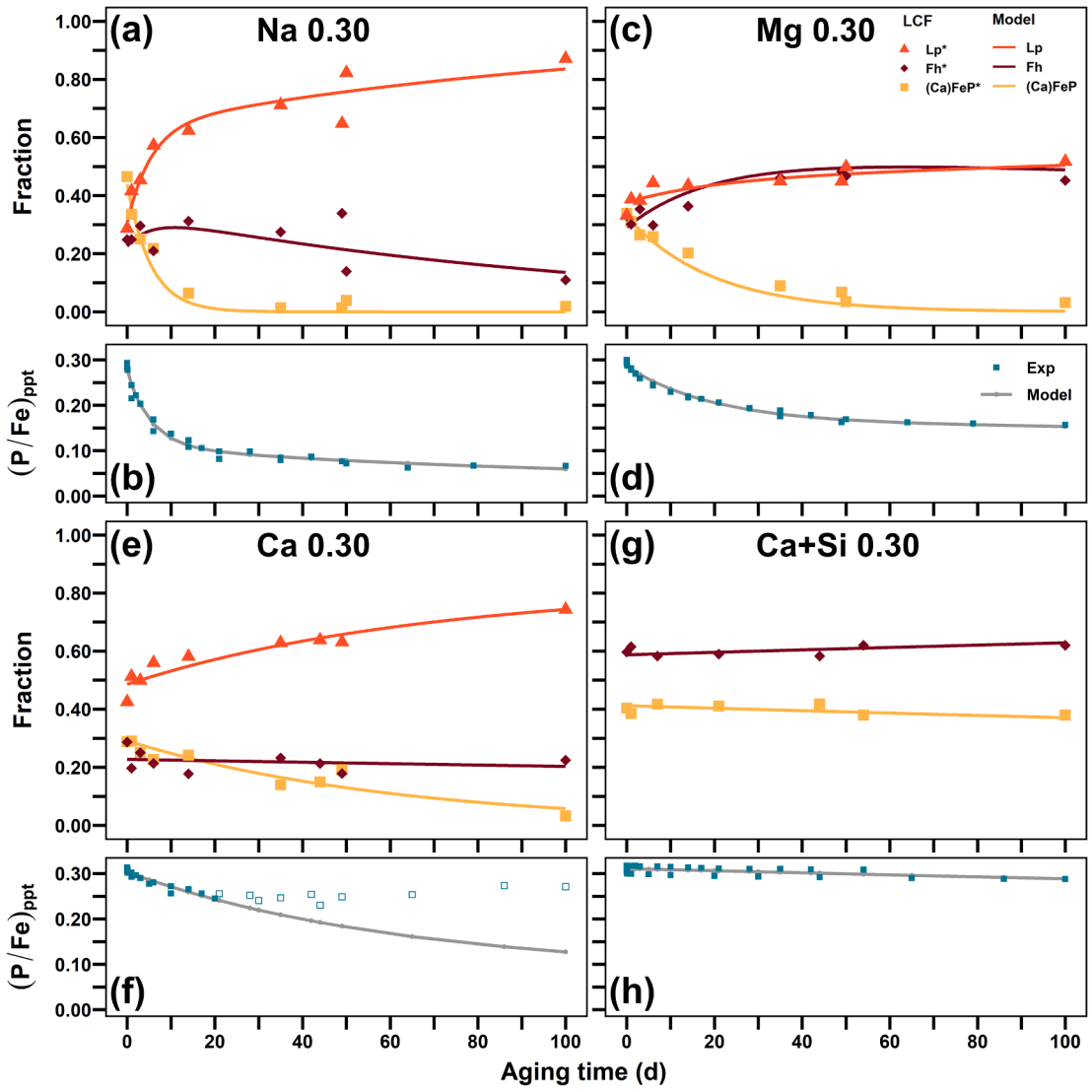

Fig. 7. Experimental and modelled Fe(III)-precipitate fractions and solution-derived $(P/Fe)_{ppt}$ as a function of aging time for the treatments Na 0.30 (a, b), Mg 0.30 (c, d), Ca 0.30 (e, f) and Ca + Si 0.30 (g, h). Experimental data (symbols) and model calculations (lines). Model calculations based on first-order transformation kinetics for (Ca)FeP* into Fh*, (Ca)FeP* into Lp*, and for Fh* into Lp*, and on constant (P/Fe) for each precipitate fraction. Fit parameters are listed in Table 3. Fit approach is described in text and in SM section S6. The data and model fits for all treatments are shown in Figs. S12 and S13. Experimental data after 20d (open symbols) in (f) were excluded from the fit for $(P/Fe)_{ppt}$ calculation.

with *k* denoting first order reaction rate coefficients. Assuming that each precipitate fraction in each treatment was characterized by a (P/Fe) ratio that remained constant during aging, the bulk $(P/Fe)_{ppt}$ could be calculated from the modelled individual precipitate fractions and their (P/Fe). Parameter optimization thus included the initial fractions of (Ca)FeP, Fh and Lp in each treatment, the first-order rate coefficients *k*, and the (P/Fe) of each precipitate fraction in each treatment. Details on the model setup and the process of parameter refinement are provided in the SM section S6. Briefly, the model was first optimized by fitting the kinetic model describing the changes in precipitate fractions (optimization of the initial fractions and first order rate coefficients), and subsequently the (P/Fe) of the bulk precipitate at each sampling time in each treatment (optimization of the P/Fe of each phase fraction in each treatment). In three subsequent fits, the LCF-derived precipitate fractions and their (P/Fe) were refined simultaneously, with an increasing weight allocated to the sum of squared residuals of the modelled $(P/Fe)_{ppt}$. The optimized model parameters listed in Table 3 correspond to the average values (and standard deviations) of the four subsequent model fits.

The kinetic model parameters of the different treatments reflected the trends in precipitate structure and transformation as quantified by LCF (Fig. 6). Notably, only the treatments at $(P/Fe)_{init}$ of 0.30 without SiO_4 included three structural components and therefore three transformation reactions. Tests were done to fit the data from these treatments with two simplified models based on only two transformation reactions: (i) Consecutive transformation of (Ca)FeP into Fh and further transformation of Fh into Lp (reactions (1) and (3)). (ii) Parallel transformation of both (Ca)FeP and Fh into Lp (reactions (2) and (3)). However, the consecutive approach was found to perform poorly as it predicted an initial peaking of the Fh fractions that was not experimentally observed. The parallel approach performed better, but could not describe the increasing Fh fractions in the Mg-containing electrolytes. Accordingly, the model based on all three transformation reactions was considered to be best suited for the consistent description of all 7 treatments at $(P/Fe)_{init}$ of 0.30 without SiO_4. Nevertheless, the tests suggested that variations in the refined model parameters between these treatments should be interpreted cautiously with respect to their mechanistic implications. All other treatments involved only two structural components: Fh and Lp in the treatments without SiO_4 at $(P/Fe)_{init}$ of 0.05, and (Ca)FeP and Fh in all treatments with SiO_4, and could therefore be described with a single transformation reaction. No

Table 3
Optimized parameters for kinetic model describing the transformation of Fe(III)-precipitate fractions and their (P/Fe). Values correspond to the average from four fits in which the weights of the sum of squared residuals for precipitate fractions and for $(P/Fe)_{ppt}$ were varied (standard deviations in parentheses; <0.02 for initial fractions)) (details in SM section S6).

Electrolyte	Initial fractions			Rate coefficients k × 1000 (d^{-1})			$t_{1/2}$ (d)[a]		(P/Fe)		
	(Ca)FeP	*Fh*	*Lp*	$k_{(Ca)FeP\text{-}Fh}$	$k_{(Ca)FeP\text{-}Lp}$	$k_{Fh\text{-}Lp}$	*(Ca)FeP*	*Fh*	*(Ca)FeP*	*Fh*	*Lp*
$(P/Fe)_{init}$ 0.30											
Na	0.45	0.23	0.32	41 (±1.0)	133 (±20)	8.3 (±0.3)	4.0 (±0.5)	84 (±3.00)	0.45 (±0.01)	0.27 (±0.04)	0.02 (±0.01)
lowMg	0.38	0.23	0.39	26 (±5.0)	39 (±6.0)	2.0 (±0.9)	11 (±2.0)	422 (±226)	0.55 (±0.01)	#[c]	#[c]
midMg	0.34	0.28	0.38	23 (±4.0)	31 (±8.0)	1.0 (±0.2)	13 (±4.0)	709 (±108)	0.54 (±0.01)	#[c]	#[c]
Mg	0.33	0.30	0.37	26 (±2.0)	16 (±4.0)	0.3 (±0.6)	17 (±2.0)	(>1000) [b]	0.59 (±0.03)	#[c]	#[c]
lowCa	0.35	0.21	0.44	13 (±4.0)	32 (±1.0)	0.0 (±0.0)	16 (±2.0)	(>1000) [b]	0.63 (±0.01)	#[c]	#[c]
midCa	0.29	0.23	0.48	4.6 (±1.9)	15 (±3.0)	0.0 (±0.0)	36 (±4.0)	(>1000) [b]	0.78 (±0.01)	#[c]	#[c]
Ca	0.28	0.23	0.49	0.0 (±0.0)	15 (±0.0)	1.2 (±0.0)	46 (±0.0)	590 (±10)	0.82 (±0.01)	#[c]	#[c]
Na + Si	0.51	0.49	–	4.3 (±0.7)	–	–	165 (±26)	–	0.53 (±0.03)	0.05 (±0.03)	–
Mg + Si	0.44	0.56	–	1.7 (±0.2)	–	–	413 (±35)	–	0.65 (±0.04)	#[c]	–
Ca + Si	0.41	0.59	–	0.8 (±0.2)	–	–	883 (±249)	–	0.69 (±0.04)	#[c]	–
$(P/Fe)_{init}$ 0.05											
Na	–	0.22	0.78	–	–	68 (±3.0)	–	10 (±1.0)	–	0.09 (±0.00)	0.02 (±0.00)
lowMg	–	0.14	0.86	–	–	13 (±1.0)	–	55 (±4.0)	–	0.13 (±0.00)	#[c]
midMg	–	0.18	0.82	–	–	12 (±0.0)	–	59 (±1.0)	–	0.11 (±0.00)	#[c]
Mg	–	0.23	0.77	–	–	8.8 (±0.2)	–	79 (±1.0)	–	0.10 (±0.00)	#[c]
lowCa	–	0.10	0.90	–	–	23 (±5.0)	–	32 (±7.0)	–	0.22 (±0.01)	#[c]
midCa	–	0.13	0.87	–	–	26 (±1.0)	–	26 (±1.0)	–	0.20 (±0.00)	#[c]
Ca	–	0.21	0.79	–	–	66 (±0.0)	–	11 (±0.0)	–	0.14 (±0.00)	#[c]
Na + Si	0.12	0.88	–	–[d]	–	–	–	–	0.43 (±0.00)	0[e]	–
Mg + Si	0.13	0.87	–	–[d]	–	–	–	–	0.40 (±0.00)	0[e]	–
Ca + Si	0.15	0.85	–	–[d]	–	–	–	–	0.35 (±0.00)	0[e]	–

[a] Half-life times, $t_{1/2,(Ca)FeP} = \ln(2)/(k_{(Ca)FeP\text{-}Fh} + k_{(Ca)FeP\text{-}Lp})$, $t_{1/2,Fh} = \ln(2)/k_{Fh\text{-}Lp}$.
[b] No reliable $t_{1/2} > 1000$ d could be calculated from $k_{Fh\text{-}Lp} < 0.0007\ d^{-1}$.
[c] (P/Fe) constrained to same value for (i) Fh in Si-free treatments at $(P/Fe)_{init}$ 0.30, (ii) Lp in Si-free treatments at $(P/Fe)_{init}$ 0.30, (iii) Fh in treatments with Si at $(P/Fe)_{init}$ 0.30, and (iv) Lp in SiO_4-free treatments at $(P/Fe)_{init}$ 0.05.
[d] No rate-coefficients fit as no temporal trends in LCF fractions. [e] Fixed to zero to constrain fit and to avoid unrealistic low $(P/Fe)_{Fh}$.

significant changes in the precipitate fractions over time were observed in the SiO_4-containing electrolytes at $(P/Fe)_{init}$ of 0.05 and no transformation reactions were thus considered in these treatments.

For the treatments at $(P/Fe)_{init}$ of 0.30, the model results adequately represented the temporal changes in the LCF-fractions and bulk $(P/Fe)_{ppt}$, as shown exemplarily for the Na 0.30, Mg 0.30, Ca 0.30, and Ca + Si 0.30 treatments in Fig. 7. In the case of the Ca 0.30 treatment, the deviation between experimental and modelled $(P/Fe)_{ppt}$ after 20 d of aging was due to the onset of Ca-phosphate precipitation that was not part of the model (but reflected in the $(P/Fe)_{ppt}$ derived from solution data). Accordingly, the $(P/Fe)_{ppt}$ at aging times > 20 d were not included in parameter refinement in this treatment. The model also allowed to reproduce trends in precipitate fractions and $(P/Fe)_{ppt}$ in all other treatments at $(P/Fe)_{init}$ of 0.30 (Fig. S12). At $(P/Fe)_{init}$ of 0.05, LCF-derived precipitate fractions were also adequately modelled, but discrepancies between modelled and experimental $(P/Fe)_{ppt}$ were observed (Fig. S13), possibly because the initial increase in suspension pH from 7.0 to 7.9 induced some PO_4 desorption that could not be described by the current model that assumed a constant (P/Fe) for each Fe(III)-precipitate fraction. For the Ca 0.05 and midCa 0.05 treatments, the $(P/Fe)_{ppt}$ was only fitted for aging times up to 3 and 6 d, respectively, because the subsequent onset of calcite precipitation led to PO_4 co-precipitation. For both $(P/Fe)_{init}$, the fitted (P/Fe) ratios of the different precipitate fractions reasonably matched with expectations from previous work (Voegelin et al., 2013; Senn et al., 2015, 2017) i.e, relatively high (P/Fe) of ~0.50–0.75 for (Ca)FeP, (P/Fe) of ~0.10–0.25 for Fh, and (P/Fe) of ~0.02 for Lp.

3.5. Scanning transmission electron microscopy (STEM)

To characterize the morphology of the Fe(III)-precipitates and the spatial distribution of elements at the nanoscale, the fresh and 100-d aged samples from the Na, Mg, Ca, Na + Si, Mg + Si and Ca + Si treatments were analyzed by STEM (SE and HAADF images; elemental distribution maps derived from EDX analysis). The SE images of fresh and aged precipitates formed at $(P/Fe)_{init}$ of 0.30 and 0.05 in the Na, Ca, and Ca + Si electrolyte are shown in Fig. 8, elemental distribution maps in Fig. 9, and the corresponding HAADF images in Fig. S15. SE and EDX images for the Mg, Na + Si and Mg + Si electrolytes at both $(P/Fe)_{init}$, and HAADF images collected together with the SE images are shown in Figs. S14, S16, and S19.

3.5.1. Fresh Fe(III)-precipitates

In terms of the morphology and elemental composition of the fresh precipitates, the STEM EDX results showed that the precipitates in the SiO_4-free electrolytes at $(P/Fe)_{init}$ of 0.30 consisted of spherical (Ca)FeP particles covered with Lp sheets. At the lower $(P/Fe)_{init}$ of 0.05, the PO_4-rich precipitate cores in the SiO_4-free treatments were less pronounced but still detectable by EDX. In the SiO_4-containing electrolytes at both $(P/Fe)_{init}$, the precipitates consisted of spherical particles composed of a core of (Ca)FeP (enriched in PO_4) and a shell of Fh (containing SiO_4) whose thickness was smaller at a $(P/Fe)_{init}$ of 0.30 than 0.05.

Closer inspection of the (Ca)FeP particles in the SiO_4-free electrolytes at $(P/Fe)_{init}$ of 0.30 exhibited a particle surfaces that more closely resembled the rough surface of pure Fh than the smooth surface of pure (Ca)FeP particles reported in previous work (Kaegi et al., 2010) and confirmed by additional STEM SE data on pure Fh and (Ca)FeP (Fig. S17). This suggested that (Ca)FeP particles in fresh precipitates formed at a $(P/Fe)_{init}$ of 0.30 in the SiO_4-free electrolytes were covered with a thin layer of Fh.

3.5.2. Aged Fe(III)-precipitates

In the Na 0.30, Mg 0.30 and Ca 0.30 treatments, the data of the 100-d aged samples showed clear changes in structure and elemental composition. (Ca)FeP particles were not observed anymore, but only Lp with relatively low P/Fe. Additional higher-magnification SE images

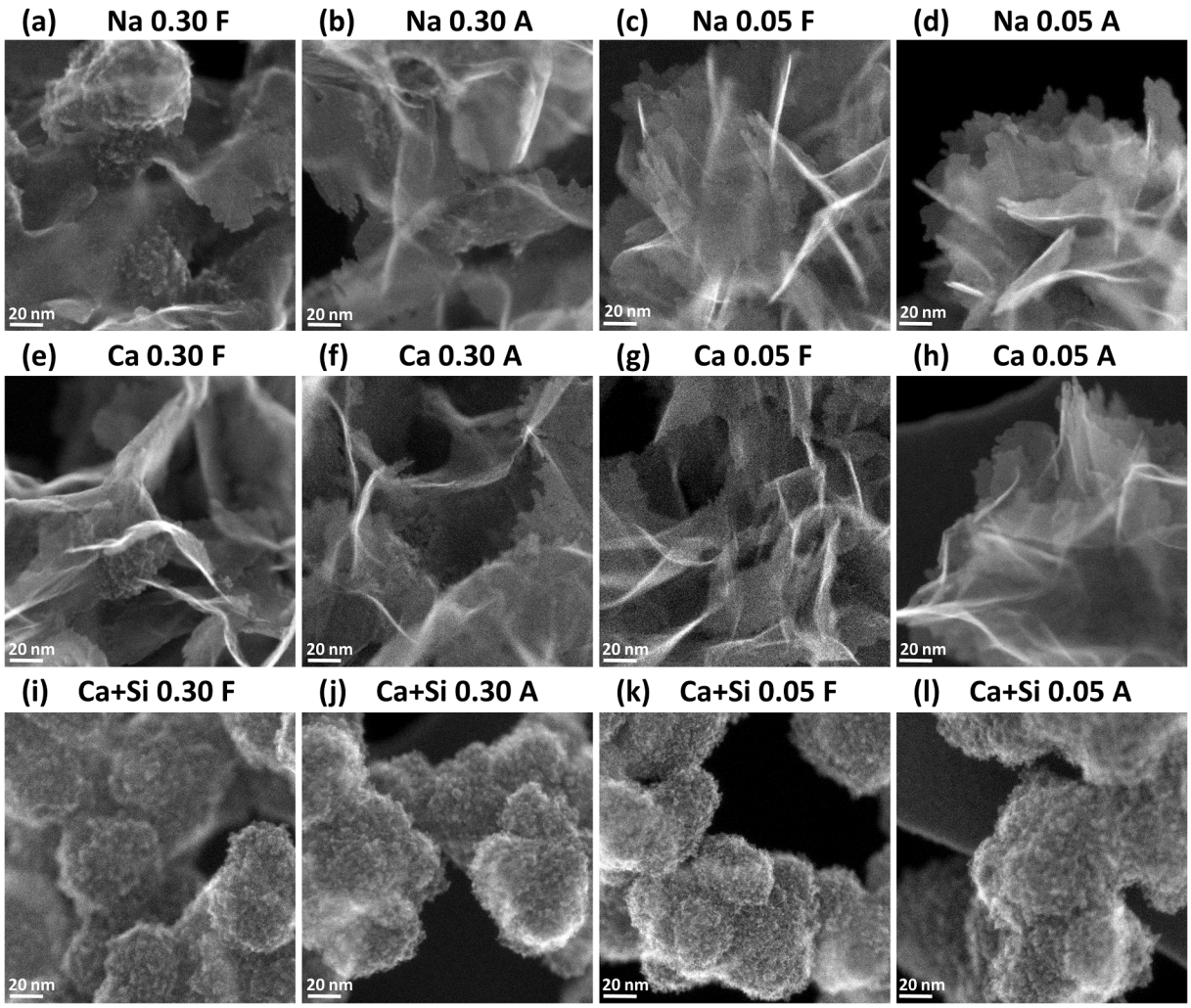

Fig. 8. Secondary electron (SE) STEM images showing the morphology of Fe(III)-precipitates freshly formed (F) and 100-d aged (A) in (a–d) Na, (e–h) Ca, and (i–l) Ca + Si electrolytes at $(P/Fe)_{init}$ of 0.30 or 0.05. High-angle annular dark-field (HAADF) images of the same sample areas are shown in Fig. S15. SE and HAADF images for precipitates from the Mg, Na + Si and Mg + Si electrolytes are shown in Figs. S14 and S16.

suggested that Lp platelets in the aged Mg 0.30 sample were covered with nanoscale Fh particles, in contrast to Lp platelets in the Na 0.30 treatment (Fig. S18). This difference was in line with the higher fraction of Fh in the 100-d aged Mg 0.30 sample than the 100-d aged Na 0.30 and Ca 0.30 samples inferred by LCF analyses, and the observation that Fh fractions were in general higher in the Mg than the Na and Ca treatments at both $(P/Fe)_{init}$ (Fig. 6). For the Na 0.05, Mg 0.05 and Ca 0.05 treatments, the EDX images (Fig. 9, Fig. S19) indicated that the PO_4-rich particle cores present in the fresh precipitates had transformed during aging, in qualitative agreement with the LCF-results (Fig. 6). For the SiO_4-containing electrolytes at both $(P/Fe)_{init}$, the STEM results did not reveal visible morphological or compositional changes from the fresh to the 100-d aged samples.

3.5.3. EDX-derived element ratios of Fe(III)-precipitates

The EDX results offered insights into the composition of the individual nanoscale components of the Fe(III)-precipitates. For $(P/Fe)_{init}$ of 0.30, bulk $(P/Fe)_{ppt}$ ratios derived from EDX spectra integrated over the entire probed sample areas showed a reasonable agreement with $(P/Fe)_{ppt}$ derived by acid digestion (Table 2). For the lower $(P/Fe)_{init}$ of 0.05, on the other hand, the comparison showed larger deviations between $(P/Fe)_{ppt}$ derived from EDX data and values obtained by acid digestion of the bulk precipitates, pointing to uncertainties in the EDX quantification at low P/Fe. Overall, however, the comparison of EDX-derived and acid digestion-derived $(P/Fe)_{ppt}$ suggested that P/Fe ratios obtained from EDX data over selected sample areas could be semi-quantitatively interpreted. Selected results for the fresh precipitates are provided in Table 4, the complete results are listed in Tables S10 and S11. In the treatments without SiO_4, the (P/Fe) were determined for the PO_4-rich particles in the center of aggregates and for Lp crystallites. In the treatments with SiO_4, the (P/Fe) were determined for the (Ca)FeP cores of the particles and for the SiO_4-containing Fh coatings. As described in Table 4, a correction was applied to the $(P/Fe)_{(Ca)FeP}$ of the (Ca)FeP cores to account for the attenuation of the P signal by the Fh shell. Conversely, in the case of the Lp platelets and Fh coatings, minor P signal contributions from PO_4-rich particles may affect the measured (P/Fe) ratios.

3.5.4. STEM-EDX data for Ca-precipitates in aged Ca-containing electrolytes

Elemental distribution maps of Ca-precipitates from the 100-d aged Ca 0.30, Ca 0.05, Ca + Si 0.30, and Ca + Si 0.05 suspensions are shown in Fig. 10. For the Ca 0.30 treatment, the data shows a Ca-phosphate particle next to Lp (as also seen in Fig. 9f). The morphology of the particle pointed to an amorphous precipitate and EDX quantification returned a molar P/Ca ratio of 0.71 (±0.01; standard deviation from quantification on three areas within particle), close to the P/Ca ratio of 0.73 (±0.02) of the Ca-phosphate particle in Fig. 9f. In the Ca 0.05

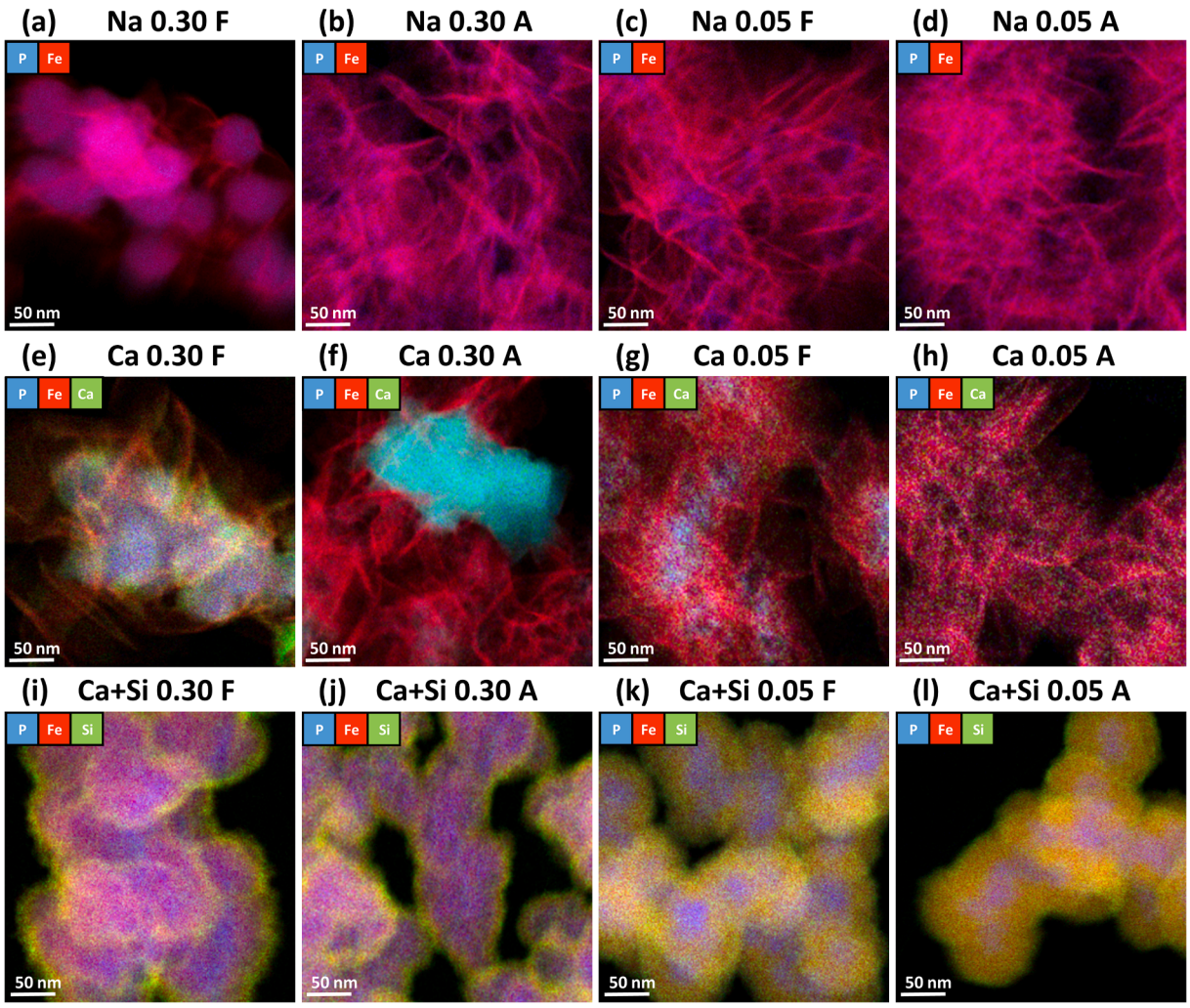

Fig. 9. Energy-dispersive X-ray (EDX) elemental distribution maps of freshly formed (F) and 100-d aged (A) Fe(III)- and Ca-precipitates in (a-d) Na, (e-h) Ca, and (i-l) Ca + Si electrolytes at $(P/Fe)_{init}$ of 0.30 (ab, ef, ij) or 0.05 (cd, gh, kl). EDX elemental distribution maps for precipitates from the Mg, Na + Si and Mg + Si electrolytes are shown in Fig. S19. Elemental ratios from EDX analyses are given in Tables S10 and S11; selected values in Table 4.

Table 4
Molar (P/Fe) ratios of individual structural units in fresh Fe(III)-precipitates (0 d) determined by STEM-EDX analyses. Coherent scattering domains (CSD) of Lp 020 XRD peak of fresh (0 d) and aged (100 d) precipitates. Si/Fe ratios of fresh and aged precipitates in SiO_4 containing treatments. Full CSD results are tabulated in Table S7. The complete STEM-EDX results are listed in Tables S10 and S11. Complete acid digestion results are listed in Tables S4 and S5.

Electrolyte	$(P/Fe)_{init}$ 0.30				$(P/Fe)_{init}$ 0.05			
	Fresh			Aged	Fresh			Aged
	STEM-EDX		XRD		STEM-EDX		XRD	
	$(P/Fe)_{(Ca)FeP}$	$(P/Fe)_{Fh}$	CSD (nm)		$(P/Fe)_{Fh}$	$(P/Fe)_{Lp}$	CSD (nm)	
Na	0.43	0.06	1.01	1.80	0.16	0.05	1.58	2.47
Mg	0.64	0.04	0.70	1.59	0.17	0.05	1.38	1.78
Ca	0.71	0.05	0.83	1.67	0.22	0.04	1.43	2.01
	STEM-EDX		Acid digestion		STEM-EDX		Acid digestion	
	$(P/Fe)_{(Ca)FeP}$	$(P/Fe)_{Fh}$	(Si/Fe)		$(P/Fe)_{(Ca)FeP}$	$(P/Fe)_{Fh}$	(Si/Fe)	
Na + Si	0.36 (0.44)[a]	0.04	0.05	0.17	0.21 (0.40)[a]	0.02	0.12[b]	0.17[c]
Mg + Si	0.42 (0.51)[a]	0.05	0.06	0.16	0.22 (0.42)[a]	0.02	0.12[b]	0.17[c]
Ca + Si	0.59 (0.72)[a]	0.07	0.06	0.17	0.25 (0.48)[a]	0.02	0.13[b]	0.18[c]

[a] For (Ca)FeP in the Si-containing treatments, the (P/Fe) ratios in parentheses were corrected for the contribution of the Fh coating around the (Ca)FeP core (assumption: Fh layer accounts for 20% of recorded signal at $(P/Fe)_{init}$ of 0.30 and for 50% of signal at $(P/Fe)_{init}$ of 0.05; based on (Ca)FeP fractions of ~50% and ~15%, respectively).
[b] Si/Fe ratios from acid digested samples after 1d aging.
[c] Si/Fe ratios from acid digested samples after 70d aging.

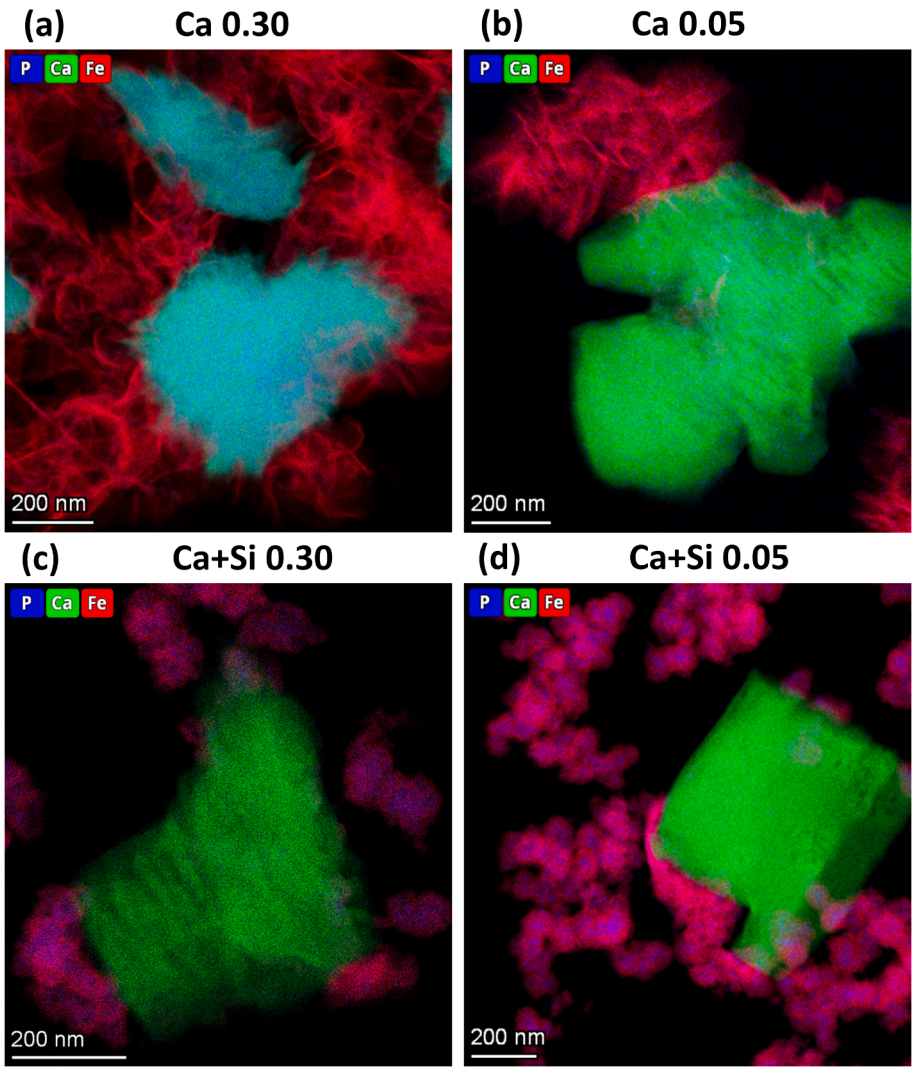

Fig. 10. EDX element distribution maps of Ca-precipitates formed in 100-d aged suspensions from the Ca 0.30 (a), Ca 0.05 (b), Ca + Si 0.30 (c), and Ca + Si 0.05 (d) treatments. EDX analysis returned P/Ca ratios of 0.72 (±0.01) (a), 0.0047 (±0.0013) (b), 0.0054 (±0.0004) (c), and 0.0004 (±0.0001) (d) (±standard deviation from the analysis of three areas within each particle).

treatment, calcite (Fig. 10b.) with a molar P/Ca ratio of 0.0047 (±0.0013) was observed next to Lp. In the Ca + Si 0.30 treatment, EDX from calcite crystal in Fig. 10c. showed a molar P/Ca ratio of 0.0054 (±0.0040). Calcite crystals with a very low P/Ca ratio (0.0004 ± 0.0001) could be observed in the Ca + Si 0.05 treatment (Fig. 10d).

4. Discussion

In the following sections, the results from this study are discussed with respect to (i) the effects of PO_4, Mg, Ca and SiO_4 on the structure and composition of the fresh Fe(III)-precipitates, (ii) the transformation of the fresh Fe(III)-precipitates during aging, (iii) effects of Fe(III)-precipitate formation and transformation on residual dissolved PO_4 over time, (iv) the interdependent formation of Ca-precipitates during suspension aging, and (v) the relevance and implications of the observed coupled processes for PO_4 immobilization in natural and engineered systems.

4.1. Structure and composition of fresh Fe(III)-precipitates formed by Fe (II) oxidation

The fresh Fe(III)-precipitates were formed by Fe(II) oxidation at $(P/Fe)_{init}$ of 0.30 and 0.05, i.e., under conditions that result in a sequential precipitation process that is expected to result in structurally heterogeneous Fe(III)-precipitates (Voegelin et al., 2013; Senn et al., 2015). In this section, the structures of the fresh precipitates as a starting point for the subsequent precipitate aging are discussed separately for SiO_4-free and SiO_4-containing electrolytes, along the individual structural units, and with special emphasis on the nanoscale heterogeneity of the precipitates as inferred from STEM analyses.

4.1.1. Fresh Fe(III)-precipitates formed in the SiO_4-free electrolytes

The structure and composition of the fresh Fe(III)-precipitates in the Na, Mg, and Ca electrolytes at $(P/Fe)_{init}$ of 0.30 and 0.05 reflected their formation via sequential precipitate formation in the absence of SiO_4. Without SiO_4, the initial formation of (Ca)FeP leads to the depletion of dissolved PO_4 and is followed by the transformation of (Ca)FeP into Fh and the precipitation of Lp during continuing Fe(II) oxidation (Voegelin et al., 2013; Senn et al., 2015). At a $(P/Fe)_{init}$ below ~0.20, this process is expected to lead to the complete transformation of initially formed (Ca)FeP into Fh over the course of Fe(II) oxidation (Voegelin et al., 2013; Senn et al., 2015). Accordingly, the fresh precipitates at $(P/Fe)_{init}$ of 0.30 contained a significant fraction of (Ca)FeP in addition to Fh and Lp, whereas the precipitates formed at $(P/Fe)_{init}$ of 0.05 consisted only of Fh and Lp, in close agreement with LCF results from previous work (Voegelin et al., 2013; Senn et al., 2015). No Goe was formed during Fe(II)

oxidation, due to effective nucleation inhibition by PO_4 (Cumplido et al., 2000; Senn et al., 2017).

4.1.1.1. (Ca-)Fe(III)-phosphate and ferrihydrite. For the fresh Na 0.30 precipitate that consisted of 46% FeP according to the LCF results, STEM-SE and HAADF images in combination with STEM-EDX data revealed the formation of spherical PO_4-rich particles with a P/Fe of ~0.43 (Figs. 8a and 9a), indicative of an amorphous Fe(III)-phosphate. Remarkably, the surface of these PO_4-rich particles more closely resembled the rough surface of Fh than the smooth surface of FeP (Kaegi et al., 2010) (Fig. 8a; see also Fig. S17). This suggested that the transformation of FeP into Fh during Fe(II) oxidation in the PO_4-depleted solution (Voegelin et al., 2013) occurred at the surface of the initially formed FeP particles and led to the formation of a surface layer of Fh. Based on LCF-derived fractions of 46% FeP and 25% Fh in the bulk Na 0.30 precipitate; corresponding to 65% FeP and 35% Fh in the spherical particles, and assuming a spherical core–shell structure, the thickness of the Fh coating was estimated to account for 14% of the particle radius.

The LCF-based fraction of (Ca)FeP decreased from the Na 0.30 (46%) over the Mg 0.30 (34%) to the Ca 0.30 (29%) precipitate. This trend was in line with previous work (Senn et al., 2015), and has been attributed to increasing PO_4 uptake into (Ca)FeP from the Na over the Mg to the Ca electrolyte, meaning that less Fe is required to deplete dissolved PO_4 and that more Fe is left to form Fh or Lp. The increase in PO_4 uptake by (Ca)FeP was confirmed by STEM-EDX, which returned P/Fe ratios of 0.43, 0,64 and 0.71 for the PO_4-rich particles in the fresh Na 0.30, Mg 0.30 and Ca 0.30 precipitates, respectively (Table 4). The enhanced uptake of PO_4 by (Ca)FeP in the Mg and especially the Ca electrolyte in comparison to the Na electrolyte has previously been attributed to favorable electrostatics in the case of bivalent electrolyte cations (Senn et al., 2015), but also the formation of ternary Fe-PO_4-Mg or Fe-PO_4-Ca complexes at the surface or in the interior of the (Ca)FeP polymers could contribute to enhanced Mg and Ca uptake (van Genuchten et al., 2014a), also considering recent results on the effects of Mg and Ca on PO_4 adsorption onto Fh (Mendez and Hiemstra, 2020). Furthermore, the formation of distinct CaFeP polymers with a local structure similar to the Ca-Fe(III)-phosphate mitridatite and possibly also Ca-phosphate polymers have previously been shown to enhance PO_4 uptake by (Ca)FeP in the Ca + Si electrolyte, as compared to the Mg electrolyte (Senn et al., 2015). In line with this interpretation, STEM-EDX showed that PO_4-rich particles contained 0.19 Mg/Fe in the Mg 0.30 precipitate and 0.53 Ca/Fe in the Ca 0.30 precipitate (Table S10), in good agreement with the composition of pure (Ca)FeP formed in Mg and Ca electrolytes at $(P/Fe)_{init}$ of 1.5; (Senn et al., 2015)). Regarding precipitate formation upon PO_4 depletion from solution, the EXAFS LCF results suggested that Fh formation was favored in the Mg 0.30 as compared to the Na 0.30 and Ca 0.30 treatments. STEM-SE images confirmed that in the fresh Mg 0.30 and Ca 0.30 samples, as in the fresh Na 0.30 precipitate, the Fh formed as coatings on the initial (Ca)FeP particles (Fig. 8ae, Fig. S14a).

In the fresh Na 0.05 precipitate dominated by Lp, SE and HAADF images did not allow to identify spherical FeP/Fh particles anymore, but the EDX elemental distribution map showed that PO_4 was still enriched in the interior of aggregates of Lp platelets, presumably in Fh particles formed by the complete transformation of FeP. Based on the P/Fe ratio of 0.16 obtained by EDX analysis in PO_4-enriched areas (potentially lowered by overlying Lp platelets), a LCF-based Fh fraction of 20%, and a P/Fe ratio of 0.044 of the bulk precipitate, a major fraction (>70%) of the total PO_4 in the fresh Na 0.05 precipitate was estimated to be concentrated in these Fh particles. The XAS and STEM data for the fresh Mg 0.05 and Ca 0.05 precipitates resembled the results for the Na 0.05 precipitate and confirmed the formation of a major fraction of Lp and some Fh. Minor differences in the LCF results among the electrolytes could only be interpreted under consideration of the aged samples, as discussed in Section 4.2.1.

4.1.1.2. Poorly crystalline lepidocrocite. For the Lp platelets formed at $(P/Fe)_{init}$ of 0.30 and 0.05 in the Na electrolyte, CSD sizes of 1.0 and 1.6 nm along the b-axis were derived from the 020 peaks of the XRD patterns (Table 4). In combination with a CSD size of 2.4 for Lp formed in PO_4-free Na electrolyte (Senn et al., 2015), these data confirmed that an increasing level of PO_4 leads to a decrease in the coherent layer stacking of Lp platelets, in line with earlier work (Cumplido et al., 2000). Regarding the Lp platelets formed in the Na, Mg and Ca electrolytes at both $(P/Fe)_{init}$, the CSD size decreased from the Na to the Ca and the Mg electrolyte (1.0, 0.8 and 0.7 nm at $(P/Fe)_{init}$ of 0.30; 1.6, 1.5 and 1.4 nm at $(P/Fe)_{init}$ of 0.05; Table 4). These trends suggested that Mg and Ca, in addition to PO_4, affected Lp crystallinity (for further discussion see section 4.2.1.3). Considering that Lp may form via green rust-like Fe(II/III)-polymers (Schwertmann and Fechter, 1994; Cumplido et al., 2000), and that structurally analogous pyroaurite-type layered double hydroxide (LDH) can form by the oxidation of Fe(II) in Mg- and bicarbonate-containing solutions (Hansen and Taylor, 1990; Hansen and Koch, 1995; Génin et al., 2005), the stronger effect of Mg than Ca could be due to Mg incorporation into intermediary Mg-Fe(II/III)-polymers. Since 6-fold coordinated Mg^{2+} has a larger ionic radius than Fe^{3+} (Shannon, 1976) and is not expected to enter the Lp structure, the formation of such Mg-containing polymers could interfere with the crystallization of Lp via oxidation of a green rust-like precursor phase.

STEM showed that the Lp platelets in all examined samples formed hedgehog-like aggregates around the initially formed FeP/Fh particles, in line with observations in earlier studies (Kaegi et al., 2010; Voegelin et al., 2013; Senn et al., 2015). This observation suggests that the Lp platelets did not form in parallel to the transformation of (Ca)FeP into Fh during continuing Fe(II) oxidation, but only once the formation of PO_4-sorbed Fh had decreased dissolved PO_4 to levels that allowed for Lp precipitation. Under these conditions, the formation of Lp platelets during the last phase of Fe(II) oxidation could have been initiated by Fe(II)-catalyzed transformation of Fh (Pedersen et al., 2005; Sheng et al., 2020) at the surface of the core/shell FeP/Fh particles, possibly followed by further Lp growth via heterogeneous surface-catalyzed Fe(II) oxidation.

4.1.2. Fresh Fe(III)-precipitates formed in the SiO_4-containing electrolytes

At an $(Si/Fe)_{init}$ of 1.0, sequential precipitate formation resulted in fresh Fe(III)-precipitates that consisted of (Ca)FeP and Fh arranged in particles with a core/shell structure. The precipitates contained no Lp, in line with earlier work indicating the effective suppression of Lp formation by SiO_4 (Schwertmann et al., 1984; Voegelin et al., 2010; Senn et al., 2015). Higher fractions of (Ca)FeP were observed in the precipitates from the Na + Si, Mg + Si and Ca + Si electrolytes than in the precipitates from the corresponding SiO_4-free treatments (Fig. 6), in line with trends reported in earlier work (Senn et al., 2015). This difference shows that SiO_4 inhibits the transformation of (Ca)FeP into Fh during continuing Fe(II) oxidation, most probably by promoting the formation of SiO_4-loaded Fh and thereby inhibiting freshly released dissolved Fe(III) to react with the (Ca)FeP. At the $(P/Fe)_{init}$ of 0.30, the fraction of (Ca)FeP decreased from the Na + Si 0.30 (53%) over the Mg + Si 0.30 (45%) to the Ca + Si 0.30 (40%) precipitate, in line with enhanced PO_4 uptake per Fe along the same sequence, as discussed for (Ca)FeP formed in the SiO_4-free treatments.

STEM-EDX data showed that individual precipitate particles consisted of a core of (Ca)FeP that was coated by SiO_4-containing Fh, in line with earlier SEM-EDX results for an analogously formed Ca + Si 0.19 precipitate (Senn et al., 2015). Furthermore, EDX analyses on the (Ca)FeP cores confirmed that the P/Fe increased from Na + Si 0.30 over Mg + Si 0.30 to Ca + Si 0.30 (Table 4). The core–shell structure of the Fe(III)-precipitate particles further suggested that the aggregation of polymers into particles proceeded rapidly in relation to the oxidation of Fe(II), such that the spatial structure of the particles mirrored the temporal sequence of precipitate formation. Assuming an identical density (per Fe) for (Ca)FeP and Fh, an approximate (Ca)FeP fraction of 50% at

$(P/Fe)_{init}$ of 0.30 and of 15% at $(P/Fe)_{init}$ of 0.05 (based on LCF results), and spherical core/shell structure, the (Ca)FeP cores were estimated to account for about 80% of the total particle diameter at $(P/Fe)_{init}$ of 0.30 and 50% of the total particle diameter at $(P/Fe)_{init}$ of 0.05, in qualitative agreement with the thickness of the SiO_4-containing Fh layer observed in the EDX elemental maps (Fig. 9i–l; Fig. S19e–l).

4.2. Transformation of Fe(III)-precipitates during aging

The time-resolved data on the transformation of the fresh Fe(III)-precipitates during aging are discussed in separate sections for experiments without and with SiO_4. This discussion is based on the nanoscale structural characterization of the aged solids and the first-order rate coefficients for individual Fe(III)-phase transformations and (P/Fe) ratios of individual precipitate fractions derived from the kinetic model.

Considering that the oxidation of Fe(II) at pH 7.0 should be completed after a reaction period of 4 h and that precipitate formation was followed by air purging to raise the pH to 7.9 prior to aging, we presume that the observed Fe(III)-precipitate transformations during aging in the dark occurred in the absence of Fe(II)-catalyzed transformation processes (Pedersen et al., 2005; Sheng et al., 2020). Since no new Fe(III) mineral phases formed during aging, Fe(III)-precipitate transformations were limited to transformations among the Fe(III)-precipitate types that had initially formed during Fe(II) oxidation.

4.2.1. Transformation of Fe(III)-precipitates during aging in SiO_4-free electrolytes

Structural data for Fe(III)-precipitates in the SiO_4-free electrolytes provided evidence for the transformation of (Ca)FeP into Fh and Lp and of Fh into Lp during aging, as well as for the further growth and crystallization of Lp. These processes are separately discussed in the following sections.

4.2.1.1. Transformations of (Ca)FeP into Fh and Lp at $(P/Fe)_{init}$ of 0.30.

In the fresh precipitates formed at $(P/Fe)_{init}$ of 0.30, core/shell (Ca)FeP/Fh particles were identified by STEM-SE and EDX data (Figs. 8ae, 9ae, S14a, S19a). After aging for 100 d, these PO_4-rich particles had disappeared, and the remaining residual solid-phase PO_4 was nearly uniformly distributed over the Fe(III)-precipitate (Figs. 8bf, 9bf, S14b, S19b). In line with these microscopic observations, the EXAFS data confirmed the transformation of (Ca)FeP into Fh or Lp during aging (Fig. 6).

The transformation of (Ca)FeP into Fh may partly have proceeded within the hydrated (Ca)FeP particles via continuing Fe(III) polymerization and Ostwald ripening of the oligomeric Fe(III) (Mao et al., 2012; Hiemstra and Zhao, 2016; Hiemstra et al., 2019). This process would have resulted in the concomitant release of PO_4. The microscopic results, however did not allow to draw any firm conclusions on the importance of this pathway. Alternatively, (Ca)FeP could transform via its dissolution, followed by the precipitation of PO_4-saturated Fh or the growth of Lp crystallites that had formed during Fe(II) oxidation. Microscopic evidence for the neoformation of Fh away from the original core/shell FeP/Fh particles was obtained for the 100-d aged precipitates formed in the Mg 0.30 treatment, where STEM-SE showed that the Lp platelets were covered with small Fh particles (Fig. S18). Similarly, Lp platelets covered with Fh particles have previously been observed to form from FeP in analogous aging experiments in Na electrolyte at a $(P/Fe)_{init}$ of 0.50 (Senn et al., 2017).

The transformation of (Ca)FeP into Fh and Lp proceeded fastest in the Na 0.30 treatment, with a 3 times lower rate coefficient for FeP transformation into Fh than Lp (Table 3). Since the transformation of (Ca)FeP into both Fh and Lp was described by first order rate equations, the overall transformation rate of (Ca)FeP corresponded to the sum of the two rate coefficients, from which the half-live time of (Ca)FeP ($t_{1/2,(Ca)FeP}$) could be derived (Table 3). For the Na 0.30 treatment, this calculation returned a $t_{1/2,FeP}$ of only 4 d, in line with rapid FeP transformation dynamics in Na electrolyte reported in previous work (Mayer and Jarrell, 2000; Voegelin et al., 2013; Senn et al., 2017).

Increasing levels of Mg in the Mg-containing electrolytes decreased the overall transformation rate of the FeP into Fh and Lp, as reflected in the increase in $t_{1/2,(Ca)FeP}$ with increasing Mg concentration (Table 3). This could be attributed to the stabilization of Mg-containing FeP by electrostatic effects or the formation of ternary Mg-PO_4-Fe complexes within the FeP; based on observations on the uptake of PO_4 by Fh in the presence of Mg or Ca (Mendez and Hiemstra, 2020). At the same time, the comparison of the rate coefficients suggested that with increasing Mg concentration, an increasing share of the FeP transformed into Fh rather than Lp. This trend could partly be attributed to the stabilization of PO_4-sorbed Fh by Mg (see section 4.2.1.2), but probably also reflected an increasing inhibition of Lp formation at increasing levels of Mg (see section 4.2.1.3).

Increasing levels of Ca in the Ca-containing electrolytes reduced the overall rate of (Ca)FeP transformation even more than Mg, as seen in the corresponding increase in $t_{1/2,(Ca)FeP}$ (Table 3). This difference between Ca and Mg was attributed to the structural uptake of Ca into amorphous (Ca)FeP with a short-range structure similar to mitridatite (Senn et al., 2015), in addition to electrostatic effects and ternary complex formation as inferred to explain the stabilizing effect of Mg. Contrary to Mg, increasing levels of Ca strongly favored (Ca)FeP transformation into Lp relative to Fh. This difference could be explained by the effective inhibition of (Ca)FeP polymerization into Fh by structural Ca (Senn et al., 2017), but could also have been linked to PO_4 uptake into Ca-phosphate during precipitate aging (see section 4.4) and the resulting destabilization of Fh (see section 4.2.1.2).

4.2.1.2. Transformation of Fh into Lp.

In the fresh Fe(III)-precipitates, Fh formed during Fe(II) oxidation was microscopically identified as a surface layer of core/shell (Ca)FeP/Fh particles at $(P/Fe)_{init}$ of 0.30 and as PO_4-enriched Fh at $(P/Fe)_{init}$ of 0.05, in both cases surrounded by Lp platelets. At the $(P/Fe)_{init}$ of 0.30, additional Fh could form during aging by the transformation of (Ca)FeP.

Comparing the rate coefficients for Fh transformation into Lp at $(P/Fe)_{init}$ of 0.30 and 0.05, Fh in general was seen to be more stable at the higher $(P/Fe)_{init}$ of 0.30. This was attributed to the higher PO_4-loading of Fh at $(P/Fe)_{init}$ of 0.30 than 0.05, considering that both PO_4 and AsO_4 have been shown to retard Fh transformation into well-crystalline Fe oxides (Paige et al., 1997; Ford, 2002). Indeed, for $(P/Fe)_{init}$ of 0.30, the kinetic model returned a P/Fe 0.27 for Fh, closely matching with the commonly observed sorption capacity of 0.25 oxyanions per Fe of Fh (Fuller et al., 1993; Gerke, 1993; Paktunc et al., 2008; Mao et al., 2012), whereas for $(P/Fe)_{init}$ of 0.05, lower P/Fe values of 0.09 (Na) to 0.22 (lowCa) were derived (0.14 ± 0.05 ($n = 7$); Table 3). In addition to PO_4-loading, however, also the type of background electrolyte cation affected the rate of Fh transformation into Lp.

In the Na and the Mg-containing electrolytes, the rate coefficient decreased with increasing Mg concentration at both $(P/Fe)_{init}$ (Table 3). We attribute this to the formation of stable ternary Fe-PO_4-Mg surface complexes that reduce the surface Gibbs free energy of Fh (Mendez and Hiemstra, 2020), and thereby stabilize Fh (formed during Fe(II) oxidation and by FeP transformation during aging) against transformation into Lp. In addition, Mg may also have induced an apparent increase in Fh stability by inhibiting Lp crystal growth (see section 4.2.1.3). For Ca, the kinetic results from the low Ca electrolytes (Table 3) suggested that Ca in analogy to Mg could stabilize Fh against transformation into Lp by the formation of ternary Fe-PO_4-Ca complexes. At the higher Ca concentrations of the midCa and the Ca electrolytes, on the other hand, Ca appeared to promote Fh transformation into Lp (Table 3). We attribute this to the effective stabilization of (Ca)FeP against transformation into Fh (section 4.2.1.1) and the uptake of PO_4 by Ca-phosphate ($(P/Fe)_{init}$ 0.30) or calcite ($(P/Fe)_{init}$ 0.05) (section 4.4) which reduces the

inhibiting effect of PO_4 on Fh transformation.

4.2.1.3. Growth and crystallization of Lp during aging. In all SiO_4-free electrolytes at both $(P/Fe)_{init}$, aging led to further Lp formation (Fig. 6). Additional Lp formation during aging resulted in increasing dissolved PO_4 concentrations (Fig. 1). Considering that similar levels of dissolved PO_4 effectively inhibited the nucleation of Lp during initial Fe(II) oxidation and sequential precipitate formation, we postulate that further Lp formation during aging mainly proceeded via the growth of Lp crystals that had formed during Fe(II) oxidation upon the temporary depletion of dissolved PO_4, rather than via the nucleation of new Lp crystals. The lower fractions of Lp in the aged suspensions at $(P/Fe)_{init}$ of 0.30 than 0.05, on the other hand, suggested that increasing concentrations of dissolved PO_4 could also inhibit Lp crystallite growth. No Goe was observed to form during Fe(III) precipitation and precipitate aging, which can be attributed to the inhibiting effects of PO_4 and AsO_4 (Cumplido et al., 2000; Senn et al., 2017). Considering recent results on template-assisted growth of Goe during Fe(II)-catalyzed transformation of Fh (Chen and Thompson, 2021; Notini et al., 2022) and own earlier results on the transformation of Lp into Goe in PO_4- and AsO_4-free precipitate suspensions (Senn et al., 2017), we postulate that under conditions that allow for the formation of Goe seed crystals during Fe oxidation, Goe crystals could continue to grow during aging at the expense of Lp.

During aging, not only the fractions of Lp in the SiO_4-free electrolytes increased, but also the CSD along the crystallographic b-axis (Table 4). Nevertheless, even after 100 d of aging, the Lp in all treatments was still poorly crystalline, considering that the largest observed CSD for Lp in the Na 0.05 treatment reached only 2.5 nm. As observed for the fresh precipitates, the CSD after aging was still higher at $(P/Fe)_{init}$ of 0.05 than 0.30, showing that the inhibiting effect of PO_4 on Lp crystallization (Cumplido et al., 2000) also persisted during the aging period. Furthermore, as in the fresh precipitates, the CSD of Lp at both $(P/Fe)_{init}$ decreased from the Na over the Ca to the Mg electrolyte. One possible explanation for the lower CSD of Lp in the Ca and Mg than the Na electrolytes could be that PO_4 more strongly binds to Fe oxides in the presence of Ca and Mg (Antelo et al., 2015; Mendez and Hiemstra, 2020), and thereby more effectively inhibits crystallization. Since Ca has a more favorable effect on PO_4 binding than Mg, however, one would expect this effect to increase from the Mg to the Ca electrolyte, opposite to the observed trend. This suggests that Mg additionally interferes with Lp formation via another Mg-specific mechanism, possibly the formation of dissolved Mg-Fe(III)-LDH type clusters that interfere with Lp crystal growth, in analogy to the postulated effect of Mg on Lp crystallization during Fe(II) oxidation (section 4.1.1.2). Another relevant factor could be that formation of Ca-phosphate or calcite in the Ca electrolytes reduces dissolved PO_4 concentrations and thereby weakens the effect of PO_4 on Lp crystallization.

4.2.2. Transformation of Fe(III)-precipitates during aging in SiO_4-containing electrolytes

In the SiO_4-containing electrolytes, Fe(II) oxidation led to the formation of (Ca)FeP/Fh core/shell particles (Fig. 6; Fig. 9) in which the SiO_4-containing Fh layer effectively stabilized the initially formed (Ca)FeP core during ongoing Fe(II) oxidation (see section 4.1.2). The aging experiment showed that this stabilizing effect also extended over the 100-d aging period.

At the $(P/Fe)_{init}$ of 0.30, the half-live times of (Ca)FeP in the SiO_4-containing Na + Si, Mg + Si and Ca + Si electrolytes were 41, 24 and 19 times larger than in the corresponding SiO_4-free electrolytes (Table 3), indicating the magnitude of the stabilizing effect. At the $(P/Fe)_{init}$ of 0.05, no (Ca)FeP transformation was detectable at all by XAS over the 100-d aging period (Fig. 6), suggesting that the thicker Fh layer even more effectively inhibited (Ca)FeP transformation. The extent of (Ca)FeP transformation (and PO_4 release) in the SiO_4-containing electrolytes, albeit limited, followed the same trend as a function of the electrolyte cation as in the SiO_4-free electrolytes (Na > Mg > Ca), showing that the stabilizing effects of the Fh layer and the electrolyte cation were additive.

The transformation of (Ca)FeP in the core of (Ca)FeP/Fh particles required the transfer of released PO_4 through the Fh layer into solution. For the Na + Si 0.30 treatment where FeP transformation was most intense and 28% of the total PO_4 were released back into solution over 100 d (Table 1), STEM-EDX images and line scans indeed indicated that PO_4 was translocated away from the FeP core into the Fh shell (Fig. S21) during aging, supporting the hypothesis that the stabilization by the Fh layer was due to inhibited PO_4 transfer out of the (Ca)FeP core. Acid digestion results further showed that the Si/Fe ratios of the precipitates even increased during aging (Table 4; Tables S4 and S5). This was most probably due to ongoing SiO_4 polymerization in the Fh layer (Swedlund et al., 2010; Swedlund et al., 2011), that may have further inhibited PO_4 transfer. The importance of the SiO_4 was also indicated by the observation that the PO_4-containing Fh layer around (Ca)FeP in the SiO_4-free electrolytes did not have the same inhibiting effect.

4.3. Solid-phase P/Fe ratios and residual dissolved PO_4

4.3.1. Solid-phase (P/Fe) ratios of individual Fe(III)-precipitate fractions

In this study, solid-phase (P/Fe) ratios of individual precipitate fractions were determined in two independent ways: First by linking EXAFS-derived Fe(III)-precipitate fractions and solution-derived bulk (P/Fe) ratios in the kinetic model to derive the (P/Fe) of the individual EXAFS-derived structural units (Table 3), and second by direct quantification of the (P/Fe) of individual structural units identified by STEM-EDX (Table 4; complete results in Tables S10 and S11). In the kinetic model, the assumption of constant P/Fe ratios for a given precipitate fraction in each treatment was a simplification, considering that the composition of amorphous basic (Ca-)Fe(III)-phosphate varies as a function of solution pH and the concentrations of Fe and PO_4 (Luedecke et al., 1989; Baken et al., 2016; van der Grift et al., 2016), and that the extent of PO_4 adsorption onto Fh and Lp depends on the dissolved PO_4 concentration (Mendez and Hiemstra, 2020). In the case of the STEM-EDX derived P/Fe ratios, on the other hand, potential signal contributions of structural units with lower or higher P/Fe than the targeted unit may have had an impact on the results (underestimation of the P/Fe of units with a higher P/Fe and overestimation of the P/Fe of units with a low P/Fe). Despite these methodological constraints, the P/Fe ratios derived by both methods in general showed analogous trends and confirmed that structural transformations of Fe(III)-precipitate types with higher PO_4 uptake per Fe into Fe(III)-precipitates with lower PO_4 uptake, i.e., of (Ca)FeP into Fh and Lp and of Fh into Lp, were the major driving force for PO_4 release over time. However, it should be noted that (P/Fe) ratios for individual precipitate types as reported in this work do not allow to calculate residual dissolved PO_4 concentrations via reaction equilibria, as would be required to quantify variations in dissolved PO_4 concentrations or to account for the competitive uptake of other oxyanions. For this purpose, the uptake of PO_4 and other oxyanions by the different Fe(III)-precipitate types would need to be quantified using surface complexation models (Hiemstra and Zhao, 2016; Senn et al., 2018), which was beyond the scope of the current work.

4.3.2. Dissolved PO_4 over time

Immediately after Fe(II) oxidation, higher fractions of residual dissolved PO_4 were observed in the SiO_4-free electrolytes at $(P/Fe)_{init}$ of 0.05 than 0.30. This trend was in line with observations in previous work (Senn et al., 2015) and suggested that within this range of $(P/Fe)_{init}$ values, increasing PO_4 levels promoted the precipitation of (Ca)FeP and Fh (Fig. 6) instead of Lp and thereby caused more effective PO_4 uptake (in terms of the fraction of total PO_4). After 100 d of aging, the trend was reverted and higher fractions of dissolved PO_4 were observed at $(P/Fe)_{init}$ of 0.30 than 0.05. This change was in line with the

transformation of (Ca)FeP into Fh and Lp and a concomitant shift to PO_4 adsorption onto Fh and Lp as the process controlling dissolved PO_4 levels. Despite the persistence of the (Ca)FeP in the Si-containing electrolytes during aging, dissolved PO_4 fractions after 100 d was also higher in the electrolytes at $(P/Fe)_{init}$ of 0.30 than 0.05, pointing to PO_4 adsorption onto the Fh shell of the core/shell particles as dissolved concentration-controlling process.

At both $(P/Fe)_{init}$, increasing levels of Mg in the electrolytes induced a pronounced decrease in residual dissolved PO_4 in the fresh precipitate suspensions (Table 1). As previously discussed in the section 4.2. for the Mg effect on precipitate transformation and crystallization, this could be related to electrostatically enhanced PO_4 uptake into Fe(III)-phosphate (Senn et al., 2015), enhanced formation of Fh with increasing Mg concentration (Fig. 6), and potentially also enhanced PO_4 adsorption onto Fh and Lp due to electrostatic effects of Mg and the formation of ternary PO_4-Mg complexes on the Fe(III)-mineral surfaces (Mendez and Hiemstra, 2020). During aging, increasing levels of Mg resulted in more effective PO_4 retention in the solid phase. This could partly be attributed to the enhanced formation ($(P/Fe)_{init}$ of 0.30) or stabilization ($(P/Fe)_{init}$ of 0.05) of Fh at the expense of Lp in the aged precipitates (Fig. 6), but also to stronger PO_4 binding on Fh and Lp.

The lowCa electrolytes at both $(P/Fe)_{init}$ showed similar trends in residual dissolved PO_4 in the fresh precipitate suspensions and during aging as the lowMg electrolytes, also when compared to the Na electrolytes. This indicated that at a Ca concentration of 0.4 mM, too low for calcite or Ca-phosphate precipitation under the given conditions, bivalent Ca and Mg affected Fe(III)-precipitate structure and PO_4 sorption in similar ways. However, at higher levels of 1.2 and 4.0 mM Ca, and especially after aging, the markedly lower residual dissolved PO_4 concentrations in the Ca-containing than the corresponding Mg-containing electrolytes indicated more effective PO_4 retention in the solid phase. These differences could be attributed to more effective binding of PO_4 by Ca-Fe(III)-phosphate than Fe(III)-phosphate and the higher stability of Ca-Fe(III)-phosphate during aging, as well as to the stronger effect of Ca than Mg onto PO_4 adsorption onto ferrihydrite that has previously been attributed to the formation of more stable ternary PO_4-Ca than PO_4-Mg complexes (Antelo et al., 2015; Mendez and Hiemstra, 2020). In addition, these discrepancies could also be linked to the co-precipitation of PO_4 with calcite or Ca-phosphate as further discussed in section 4.4.

Shortly after Fe(II) oxidation in the fresh SiO_4 containing electrolytes, the residual dissolved PO_4 levels were substantially lower than in the corresponding SiO_4 free electrolytes due to the stabilizing effect of SiO_4 on the (Ca-)Fe(III)-phosphate, and due to promotion of Fh instead of Lp formation and thus a higher sorption capacity of the resulting Fe (III)-precipitates. During the aging of the SiO_4-containing suspensions, only limited PO_4 release was observed in all treatments at $(P/Fe)_{init}$. Its relative extent showed the same dependence on the electrolyte cation (Na > Mg > Ca) as in the SiO_4-free treatments, indicating that the effects of the electrolyte cations and SiO_4 on PO_4 retention were mutually additive. At the $(P/Fe)_{init}$ of 0.05, only minimal PO_4 releases were observed over 100-d, in line with undetectable changes in Fe(III)-coordination (Fig. 6).

4.4. *Formation of Ca-carbonate and Ca-phosphate phases and their effects on PO_4*

The formation of Ca-carbonate and Ca-phosphate in the Ca-containing electrolytes and its coupling to Fe(III)-precipitate dynamics are discussed in the following section based on data on changes in dissolved Ca and PO_4 and solution pH over time (Figs. 1 and 2), saturation indices of Ca-carbonates and –phosphates in the aging suspensions (Tables S12 and S13, and compositional and structural information from XRD (Figs. 3, S5 and S6), FTIR (Figs. 4, S7 and S8) and STEM (Fig. 10) analyses.

4.4.1. *Formation of Ca-carbonate and its effect on dissolved PO_4*

At their initial pH of 7.0, the Ca-containing electrolytes at their nominal Ca concentrations were weakly supersaturated or undersaturated with respect to calcite (SI 0.4 for Ca and Ca + Si, −0.1 for midCa and −0.6 for lowCa electrolytes). Upon the increase in suspension pH to 7.9 by CO_2 purging with air, all Ca-containing electrolytes became supersaturated with respect to calcite, with SI of 1.3, 0.8 and 0.3 for the Ca/Ca + Si, midCa and lowCa electrolytes, respectively. Precipitation of calcite upon CO_2 outgassing generally occurs in natural waters when its

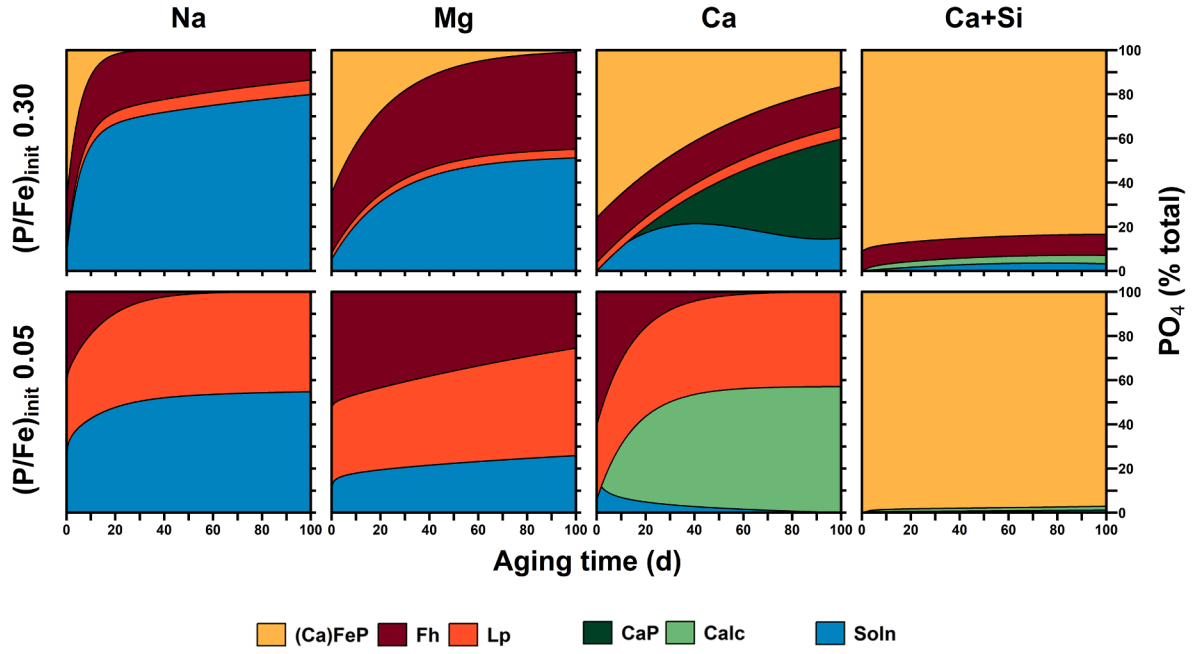

Fig. 11. Schematic depiction of changes in the fractions of dissolved PO_4 (blue), Fe(III)-precipitate-associated PO_4 (orange-brown colors), and Ca-precipitate associated PO_4 (green colors) over the course of suspension aging. Dissolved PO_4 was based on interpolations of measured data, Ca-precipitate associated PO_4 was based on an interpolation of the increase in precipitated Ca and the identification of Ca-phases and their P/Ca by XRD, FTIR and STEM-EDX, and the Fe(III)-precipitate-associated fractions were obtained from the kinetic model (based on EXAFS data and solution-derived P/Fe ratios).

SI exceeds 0.8 (Merz-Preiß and Riding, 1999). Accordingly, calcite precipitation upon CO_2 outgassing could theoretically occur in the Ca/Ca + Si and midCa electrolytes in the absence of interfering ions such as PO_4. In the presence of dissolved PO_4, however, the formation and growth of Ca-carbonate crystals is slowed down or completely inhibited (Reddy, 1977; House, 1987). At low PO_4 concentrations, PO_4 adsorbed onto the surface of calcite is occluded by layerwise calcite growth, leading to the co-precipitation of PO_4 with calcite (House and Donaldson, 1986; House, 1990). Higher dissolved PO_4 concentrations lead to a higher saturation of calcite growth sites and a slowing down of calcite precipitation, with complete inhibition of calcite formation and growth at PO_4 concentrations >20 μM (House, 1990). In all Ca-containing electrolytes, right after Fe(II) oxidation, residual dissolved PO_4 concentrations were far lower than 20 μM (at most 3.5 μM; Table 1), thus theoretically allowing for the nucleation of calcite crystals in the midCa and Ca electrolytes.

At $(P/Fe)_{init}$ of 0.30 in the midCa 0.30 and Ca 0.30 treatments, however, Fe(III)-precipitate aging led to the increase in dissolved PO_4 to concentrations >20 μM within days, and thereby prevented substantial calcite precipitation and Ca removal from solution at the start of the aging phase (Figs. 2–4). Conversely, in the Ca 0.30 treatment, the onset of Ca-phosphate formation after 44 d of aging (see Section 4.4.2) led to a decrease in dissolved PO_4 to ~20 μM and allowed for the precipitation of calcite towards the end of the aging period (Fig. 2; ~6% of total Ca), similar to trends observed in an earlier aging experiment at $(P/Fe)_{init}$ ~0.30 (Senn et al., 2018) and structurally confirmed by the XRD (Fig. 3) and FTIR results (Fig. 4). In the Ca + Si 0.30 treatment, on the other hand, dissolved PO_4 was effectively retained by the Fe(III)-precipitate formed in the presence of SiO_4, and calcite precipitation started at the onset of suspension aging, as reflected in the decrease of dissolved Ca and pH (Fig. 2ac) and in the XRD (Fig. 3, Fig. 11), FTIR (Fig. 4) and STEM (Fig. 10) results. STEM-EDX indicated a molar P/Ca ratio of 0.0054 for calcite formed in the Ca + Si 0.30 treatment. Combined with the observed decrease in dissolved Ca (Fig. 2), this corresponded to ~4.5% of the total PO_4, similar to the fraction of PO_4 released into solution over 100 d (3.9%, Table 1).

At $(P/Fe)_{init}$ of 0.05, dissolved PO_4 concentrations in the Ca 0.05 and midCa 0.05 treatments were very low after Fe(II) oxidation and did not exceed 5.2 μM during aging (Table 1, Fig. 1). Consequently, calcite formation was not fully inhibited and dissolved Ca concentrations were observed to decrease over time (Fig. 2). Concomitantly, PO_4 concentrations started to decrease again after ~3 and 20 days in the Ca 0.05 and midCa 0.05 treatments due to PO_4 co-precipitation with calcite. For the Ca 0.05 treatment, based on the STEM-EDX-derived P/Ca ratio of 0.0047 of calcite (Fig. 10) and the decrease in dissolved Ca over time (Fig. 2), ~37% of the total PO_4 were estimated to be co-precipitated with calcite after 100 d. In parallel, dissolved PO_4 decreased to 0.8 μM (3.1% of total PO_4; Table 1) by the end of the aging period. This showed that co-precipitation of PO_4 with calcite can effectively counteract PO_4 release from aging Fe(III)-precipitates and reduce dissolved PO_4 concentrations to very low levels. Effective PO_4 uptake by calcite may also have aided Fe(III)-precipitate transformation into Lp by presenting an effective PO_4 sink. In the Ca + Si 0.05 treatment, calcite formed over the entire aging period (Fig. 2, Fig. 3), together with some aragonite whose transformation into calcite may have been inhibited by SiO_4 (Kellermeier et al., 2013). Considering that aragonite can more effectively retain PO_4 than calcite (Millero et al., 2001), SiO_4 could cause enhanced PO_4 retention via its effect on Ca-carbonate formation. The STEM-EDX-derived P/Ca ratio of calcite in the Ca + Si 0.05 electrolyte was very low and should be considered with caution (0.0004; Fig. 10). Yet, in combination with the decrease in dissolved Ca (Fig. 2), we estimate that at the very low dissolved PO_4 concentrations (<0.3 μM) in this treatment, up to 3% of the PO_4 were co-precipitated with calcite (and aragonite) over 100 d.

4.4.2. Formation of Ca-phosphate and its effect on dissolved PO_4

During suspension aging, formation of Ca-phosphate was only observed in the Ca 0.30 treatment, and was reflected in a decrease in dissolved PO_4 after 44 days of aging (Fig. 1). Based on FTIR (Fig. 4) and STEM-EDX (Fig. 10, Table S10) results, the Ca-phosphate was identified as amorphous calcium phosphate (ACP) with a P/Ca of ~0.72, a molar ratio close to ACP (0.74) (Christoffersen et al., 1990) and intermediate between octacalcium phosphate (OCP; P/Ca 0.75) and beta-tricalcium phosphate (β-TCP; P/Ca 0.67) (Wang and Nancollas, 2008).

The formation of Ca-phosphates at pH 7–9 is supposed to proceed via the nucleation of ACP, followed by its dissolution and re-precipitation into secondary ACP or OCP and, eventually, hydroxyapatite (HAP) (Feenstra and De Bruyn, 1979; Christoffersen et al., 1990; Wang and Nancollas, 2008). Dissolved ions (including HCO_3^-) can interfere with the nucleation and precipitation of Ca-phosphate (Cao and Harris, 2008). In unseeded bicarbonate-containing solutions, the induction of HAP formation requires very high degrees of supersaturation (SI > 10) (Van Der Houwen and Valsami-Jones, 2001; Plant and House, 2002; Wright et al., 2011). The SI of HAP, β-TCP, OCP and ACP in all Ca-containing suspensions as a function of aging time are listed in in the SM (Tables S12 and S13). After 44 d of aging, when dissolved PO_4 started to decrease again in the Ca 0.30 treatment (Fig. 1), the Ca 0.30 suspension reached SI of 0.9 for OCP, 2.7 for β-TCP and 11.7 for HAP. Towards the end of the aging period, dissolved PO_4 stabilized at ~20 μM (Fig. 1) and the SI of OCP reached a value of 0.0 (Table S12). These trends suggested that supersaturation with respect to OCP was required to induce Ca-phosphate precipitation in our experiments, as postulated previously based on aging experiment under analogous conditions (Senn et al., 2017). Even in solutions supersaturated with respect to HAP and β-TCP, OCP has been reported to remain the preferentially growing phase (Heughebaert et al., 1983). Accordingly, the identification of the Ca-phosphate as ACP by FTIR (Fig. 4) in combination with the SI of near zero for OCP towards the end of the aging period (Table S12) may indicate that initial ACP formation transitioned into gradual but still limited ACP transformation into OCP.

The precipitation of Ca-phosphate in the Ca 0.30 electrolyte decreased the dissolved PO_4 to ~20 μM and allowed for some calcite formation towards the end of the aging phase, as confirmed by XRD (Fig. 3) and FTIR (Fig. 4) and as inferred in an earlier study (Senn et al., 2018). After 100 d of aging, 40% of the total PO_4 in the Ca 0.30 treatment were estimated to be retained in the Fe(III)-precipitate dominated by Lp (based on a P/Fe of 0.12 obtained from the kinetic model), and 13% of the total PO_4 remained dissolved. The remaining ~47% of the total PO_4 thus precipitated as Ca-phosphate with a P/Ca ratio of ~0.72. This requires ~36% of the Ca precipitated from solution in the later aging phase; in agreement with the identification of significant amounts of both ACP and calcite in the wall precipitates by FTIR (Fig. 4).

In the midCa 0.30 electrolyte, the SI of HAP, β-TCP and OCP after 100 d of aging reached similar values as in the Ca 0.30 treatment at the onset of Ca-phosphate formation around 44 d. It is therefore possible that Ca-phosphate precipitation could have set in over a longer period of time. In all other treatments, low Ca levels (lowCa electrolytes), low PO_4 levels as a consequence of effective PO_4 retention (SiO_4-containing electrolytes) or a low $(P/Fe)_{init}$ of 0.05, and lower pH values due to calcite precipitation prevented the formation of Ca-phosphate during suspension aging. Regarding the latter factor, it its noteworthy that Ca-phosphate precipitation can promote the subsequent precipitation of calcite, whereas the formation of calcite effectively prevents subsequent Ca-phosphate precipitation by reducing the concentrations of PO_4 and Ca as well as solution pH.

4.5. Environmental implications

The results of this study reveal in detail how Mg, Ca, SiO_4 and PO_4 individually and in combination affect the composition of the fresh Fe(II) oxidation products in near-neutral natural waters, their

transformation over time, the coupling with Ca-precipitation and the resulting sequestration and release of PO_4. At concentrations that are representative for anoxic groundwaters, for example groundwaters exfiltrating from agricultural soils into surface waters (Griffioen, 2006; Baken et al., 2015; Baken et al., 2016; van der Grift et al., 2016) or being used as a drinking water resource (Wolthoorn et al., 2004; Hug et al., 2008). Combining the data on changes in dissolved PO_4 over time with the results on Fe(III)- and Ca-precipitate formation and transformation, we derived schematic diagrams depicting the changes in the fractions of dissolved PO_4 and of PO_4 associated with individual solid phases over the course of 100 d of aging upon Fe(II) oxidation for selected treatments (Fig. 11). As these diagrams reveal, the direction, extent and kinetics of changes in PO_4 distribution during aging greatly vary with the level of PO_4 and the presence of Mg, Ca and SiO_4, reflecting the interdependent effects of these solutes on precipitate formation and transformation processes.

Initially, PO_4 was effectively removed by uptake into Fe(III)-precipitates formed during Fe(II) oxidation. The largest and fastest release of PO_4 during aging occurred in the Na electrolyte, where most PO_4 was released back to solution within 14 days. Most of the retained PO_4 in solids at the end of the aging period was in the residual fraction of Fh at $(P/Fe)_{init}$ of 0.30, whereas at $(P/Fe)_{init}$ of 0.05, Fh was nearly completely transformed into Lp and solid-phase PO_4 was finally mainly retained by Lp. In the presence of Mg, the extent of PO_4 release was reduced, due to enhanced sorption to the Fe(III)-precipitates and to slowed down transformation of Fh into Lp. A much different pattern was observed in the Ca electrolytes, where Ca stabilized CaFeP (at $(P/Fe)_{init}$ of 0.30) and where a significant part of the PO_4 got sequestered into CaP ($(P/Fe)_{init}$ 0.30) or calcite ($(P/Fe)_{init}$ 0.05). Towards the end of the aging period, the sequestration of PO_4 into Ca-precipitates resulted in lower dissolved PO_4 and lower Fe(III)-precipitate-associated PO_4 fractions than in the corresponding Mg electrolytes. Finally, another major change in precipitate formation and transformation dynamics was induced by the presence of SiO_4, which contributed to the stabilization of the initially formed CaFeP, and via the resulting low dissolved PO_4 levels, also enabled the continuing sequestration of low levels of PO_4 via calcite precipitation.

The initial PO_4 concentrations of 150 μM and 25 μM PO_4 employed in this study are representative for nutrient-rich anoxic groundwater, as compared to PO_4 concentrations of <1 μM deemed to limit the risk of algal blooms in surface waters (Oelkers and Valsami-Jones, 2008). In the fresh suspensions, lower PO_4 levels were observed in the SiO_4-containing treatments at both PO_4 levels, whereas higher PO_4 concentrations remained dissolved in the absence of SiO_4 (Table 1). After aging for 100 d, PO_4 concentrations <1 μM were still maintained in the SiO_4-containing treatments at $(P/Fe)_{init}$ of 0.05, whereas in the Ca + Si electrolyte at $(P/Fe)_{init}$ of 0.30, the PO_4 concentration had increased to 6 μM (Table 1). These results show that, via their combined and interdependent effects on precipitate formation and aging, Ca and SiO_4 contribute to effective PO_4 retention over extended periods of time, but that high initial $(P/Fe)_{init}$ ratios may still result in the release of significant levels of PO_4 over time, albeit at very slow rates.

Regarding the sequestration of PO_4 by Ca-precipitates, the results of this study show that PO_4 released from aging Fe(III)-precipitates can be effectively retained by co-precipitation with calcite. This process, however, can only occur where initial PO_4 removal by co-precipitation with Fe(III) results in sufficiently low dissolved PO_4 levels, for example due to the presence of SiO_4. In contrast to PO_4 associated with Fe(III)-precipitates, PO_4 co-precipitated with $CaCO_3$ is not susceptible to reductive mobilization from sediments of drainage ditches or lakes (Gächter and Müller, 2003; House, 2003; Dittrich et al., 2011; Baken et al., 2015). On the other hand, calcite-bound PO_4 can be released in environments where acidification promotes calcite dissolution (De Jonge and Villerius, 1989; Pain et al., 2020).

In previous work on the extent of PO_4 removal from nutrient-rich anoxic groundwater, the saturation index of HAP in the fully aerated groundwater (in addition to $(P/Fe)_{init}$) has been found to be a good indicator to quantify the degree of PO_4 removal within 24 h upon aeration (Griffioen, 2006). However, considering that Ca-phosphate precipitation in the current study could not reduce dissolved PO_4 to levels lower than 20 μM and that the formation of Ca-phosphate was only observed during prolonged precipitate aging, the reported relationship may rather reflect the formation of amorphous (Ca)FeP (and amorphous CaP) (Senn et al., 2015) at high Ca and PO_4 concentrations than effective PO_4-removal by HAP within a relatively short time-period upon solution aeration. In systems with high dissolved PO_4 levels and limited PO_4 removal by Fe(III)-precipitates, however, our results suggest that the formation of Ca-phosphates can contribute to PO_4 retention in the longer term.

In the present study, experiments were performed in the absence of dissolved organic carbon, which is considered to be adequate for systems characterized by low concentrations of organic ligands. However, in the presence of high levels of dissolved organic carbon, for example in drainage waters impacted by manure application or in organic-rich peatland soils and sediments (Sato et al., 2005; Gerke, 2010; Karlsson and Persson, 2010; ThomasArrigo et al., 2014; Sundman et al., 2016), organic compounds may further confound the intricate interactions that are triggered by the aeration of anoxic Fe(II) and PO_4 containing waters.

Declaration of Competing Interest

The authors declare that they have no known competing financial interests or personal relationships that could have appeared to influence the work reported in this paper.

Acknowledgements

Numa Pfenninger, Gioele Scacco, Muhammed Rezaii, and Anna Hasenfratz (Eawag, Switzerland) are acknowledged for assistance with laboratory experiments and analyses. The Light Source of the Karlsruhe Institute of Technology (KIT, Karlsruhe, Germany) and Swiss Light Source (SLS, Villigen, Switzerland) are acknowledged for providing synchrotron XAS beamtime. The Scientific Center for Optical and Electron Microscopy (ScopeM) at ETH Zurich is acknowledged for granting the access to the electron microscopy. This project was funded via the European Union's Horizon 2020 research and innovation programme under the Marie Sklodowska-Curie grant agreement No 813438 (P-TRAP).

Appendix A. Supplementary material

Supplementary material: Experimental details, element ratios of precipitates, additional plots of ICP-MS and pH data, complete sets of XRD and FTIR spectra, Fe K-edge EXAFS spectra and LCF results, details on kinetic model and model results for all treatments, complete sets of STEM data (SE, HAADF and EDX images), and saturation indices of Ca-phosphates and calcite in Ca-containing treatments are included in a single PDF document. A compilation of raw data in text format (XRD, FTIR, XAS, ICP-MS and pH) is available in a zipped folder. Supplementary material to this article can be found online at https://doi.org/10.1016/j.gca.2023.09.004.

References

Antelo, J., Arce, F., Fiol, S., 2015. Arsenate and phosphate adsorption on ferrihydrite nanoparticles. Synergetic interaction with calcium ions. Chem. Geol. 410, 53–62.
Arai, Y., Sparks, D.L., 2001. ATR–FTIR spectroscopic investigation on phosphate adsorption mechanisms at the ferrihydrite-water interface. J. Colloid Interface Sci. 241, 317–326.
Baken, S., Verbeeck, M., Verheyen, D., Diels, J., Smolders, E., 2015. Phosphorus losses from agricultural land to natural waters are reduced by immobilization in iron-rich sediments of drainage ditches. Water Res. 71, 160–170.
Baken, S., Moens, C., van der Grift, B., Smolders, E., 2016. Phosphate binding by natural iron-rich colloids in streams. Water Res. 98, 326–333.

Bargar, J.R., Kubicki, J.D., Reitmeyer, R., Davis, J.A., 2005. ATR-FTIR spectroscopic characterization of coexisting carbonate surface complexes on hematite. Geochim. Cosmochim. Acta 69, 1527–1542.
Bingham, S.T., Buss, H.L., Mouchos, E.M., Johnes, P.J., Gooddy, D.C., Bagnall, J.P., 2020. Rates of hydroxyapatite formation and dissolution in a sandstone aquifer: Implications for understanding dynamic phosphate behaviour within an agricultural catchment. Appl. Geochem. 115, 104534.
Cao, X., Harris, W., 2008. Carbonate and magnesium interactive effect on calcium phosphate precipitation. Environ. Sci. Tech. 42, 436–442.
Carlson, L.T., Schwertmann, U., 1981. Natural ferrihydrites in surface deposits from Finland and their association with silica. Geochim. Cosmochim. Acta 45, 421–429.
Châtellier, X., Grybos, M., Abdelmoula, M., Kemner, K.M., Leppard, G.G., Mustin, C., West, M.M., Paktunc, D., 2013. Immobilization of P by oxidation of Fe(II) ions leading to nanoparticle formation and aggregation. Appl. Geochem. 35, 325–339.
Chen, C., Thompson, A., 2021. The influence of native soil organic matter and minerals on ferrous iron oxidation. Geochim. Cosmochim. Acta 292, 254–270.
Christoffersen, M., Christoffersen, J., Kibalczyc, W., 1990. Apparent solubilities of two amorphous calcium phosphates and of octacalcium phosphate in the temperature range 30–42°C. J. Cryst. Growth 106, 349–354.
Combes, C., Rey, C., 2010. Amorphous calcium phosphates: synthesis, properties and uses in biomaterials. Acta Biomater. 6, 3362–3378.
Conley, D.J., Björck, S., Bonsdorff, E., Carstensen, J., Destouni, G., Gustafsson, B.G., Hietanen, S., Kortekaas, M., Kuosa, H., Markus Meier, H.E., Müller-Karulis, B., Nordberg, K., Norkko, A., Nürnberg, G., Pitkänen, H., Rabalais, N.N., Rosenberg, R., Savchuk, O.P., Slomp, C.P., Voss, M., Wulff, F., Zillén, L., 2009a. Hypoxia-related processes in the Baltic Sea. Environ. Sci. Tech. 43, 3412–3420.
Conley, D.J., Paerl, H.W., Howarth, R.W., Boesch, D.F., Seitzinger, S.P., Havens, K.E., Lancelot, C., Likens, G.E., 2009b. Controlling eutrophication: nitrogen and phosphorus. Science 323, 1014–1015.
Cornell, R.M., Schwertmann, U., 2003. The Iron Oxides: Structure, Properties, Reactions, Occurrences and Uses. John Wiley & Sons.
Cosmidis, J., Benzerara, K., Morin, G., Busigny, V., Lebeau, O., Jézéquel, D., Noël, V., Dublet, G., Othmane, G., 2014. Biomineralization of iron-phosphates in the water column of Lake Pavin (Massif Central, France). Geochim. Cosmochim. Acta 126, 78–96.
Cumplido, J., Barrón, V., Torrent, J., 2000. Effect of phosphate on the formation of nanophase lepidocrocite from Fe(II) sulfate. Clays Clay Miner. 48, 503–510.
De Jonge, V., Villerius, L., 1989. Possible role of carbonate dissolution in estuarine phosphate dynamics. Limnol. Oceanogr. 34, 332–340.
Dittrich, M., Gabriel, O., Rutzen, C., Koschel, R., 2011. Lake restoration by hypolimnetic $Ca(OH)_2$ treatment: impact on phosphorus sedimentation and release from sediment. Sci. Total Environ. 409, 1504–1515.
Dorozhkin, S.V., 2010. Amorphous calcium (ortho) phosphates. Acta Biomater. 6, 4457–4475.
Feenstra, T., De Bruyn, P., 1979. Formation of calcium phosphates in moderately supersaturated solutions. J. Phys. Chem. 83, 475–479.
Ford, R.G., 2002. Rates of hydrous ferric oxide crystallization and the influence on coprecipitated arsenate. Environ. Sci. Tech. 36, 2459–2463.
Fuller, C.C., Davis, J.A., Waychunas, G.A., 1993. Surface chemistry of ferrihydrite: Part 2. Kinetics of arsenate adsorption and coprecipitation. Geochim. Cosmochim. Acta 57, 2271–2282.
Gächter, R., Müller, B., 2003. Why the phosphorus retention of lakes does not necessarily depend on the oxygen supply to their sediment surface. Limnol. Oceanogr. 48, 929–933.
Génin, J.-M.-R., Aïssa, R., Géhin, A., Abdelmoula, M., Benali, O., Ernstsen, V., Ona-Nguema, G., Upadhyay, C., Ruby, C., 2005. Fougerite and Fe^{II-III} hydroxycarbonate green rust; ordering, deprotonation and/or cation substitution; structure of hydrotalcite-like compounds and mythic ferrosic hydroxide $Fe(OH)_{(2+x)}$. Solid State Sci. 7, 545–572.
Gerke, J., 1993. Phosphate adsorption by humic/Fe-oxide mixtures aged at pH 4 and 7 and by poorly ordered Fe-oxide. Geoderma 59, 279–288.
Gerke, J., 2010. Humic (organic matter)-Al (Fe)-phosphate complexes: an underestimated phosphate form in soils and source of plant-available phosphate. Soil Sci. 175, 417–425.
Griffioen, J., 2006. Extent of immobilisation of phosphate during aeration of nutrient-rich, anoxic groundwater. J. Hydrol. 320, 359–369.
Gunnars, A., Blomqvist, S., Johansson, P., Andersson, C., 2002. Formation of Fe(III) oxyhydroxide colloids in freshwater and brackish seawater, with incorporation of phosphate and calcium. Geochim. Cosmochim. Acta 66, 745–758.
Hansen, H.C.B., Koch, C.B., 1995. Synthesis and characterization of pyroaurite. Appl. Clay Sci. 10, 5–19.
Hansen, H.C.B., Taylor, R., 1990. Formation of synthetic analogues of double metal-hydroxy carbonate minerals under controlled pH conditions: I. The synthesis of pyroaurite and reevesite. Clay Miner. 25, 161–179.
Heughebaert, J.-C., Zawacki, S.J., Nancollas, G.H., 1983. The growth of octacalcium phosphate on beta tricalcium phosphate. J. Cryst. Growth 63, 83–90.
Hiemstra, T., Mendez, J.C., Li, J., 2019. Evolution of the reactive surface area of ferrihydrite: time, pH, and temperature dependency of growth by Ostwald ripening. Environ. Sci. Nano 6, 820–833.
Hiemstra, T., Zhao, W., 2016. Reactivity of ferrihydrite and ferritin in relation to surface structure, size, and nanoparticle formation studied for phosphate and arsenate. Environ. Sci. Nano 3, 1265–1279.
House, W.A., 1987. Inhibition of calcite crystal growth by inorganic phosphate. J. Colloid Interface Sci. 119, 505–511.
House, W.A., 1990. The prediction of phosphate coprecipitation with calcite in freshwaters. Water Res. 24, 1017–1023.
House, W.A., 2003. Geochemical cycling of phosphorus in rivers. Appl. Geochem. 18, 739–748.
House, W.A., Donaldson, L., 1986. Adsorption and coprecipitation of phosphate on calcite. J. Colloid Interface Sci. 112, 309–324.
Hug, S.J., Leupin, O.X., Berg, M., 2008. Bangladesh and Vietnam: Different groundwater compositions require different approaches to arsenic mitigation. Environ. Sci. Tech. 42, 6318–6323.
Hupfer, M., Lewandowski, J., 2008. Oxygen controls the phosphorus release from Lake Sediments–a long-lasting paradigm in limnology. Int. Rev. Hydrobiol. 93, 415–432.
Hyacinthe, C., Van Cappellen, P., 2004. An authigenic iron phosphate phase in estuarine sediments: composition, formation and chemical reactivity. Mar. Chem. 91, 227–251.
Kaegi, R., Voegelin, A., Folini, D., Hug, S.J., 2010. Effect of phosphate, silicate, and Ca on the morphology, structure and elemental composition of Fe(III)-precipitates formed in aerated Fe(II) and As(III) containing water. Geochim. Cosmochim. Acta 74, 5798–5816.
Kappler, A., Bryce, C., Mansor, M., Lueder, U., Byrne, J.M., Swanner, E.D., 2021. An evolving view on biogeochemical cycling of iron. Nat. Rev. Microbiol. 19, 360–374.
Karlsson, T., Persson, P., 2010. Coordination chemistry and hydrolysis of Fe(III) in a peat humic acid studied by X-ray absorption spectroscopy. Geochim. Cosmochim. Acta 74, 30–40.
Kellermeier, M., Glaab, F., Klein, R., Melero-Garcia, E., Kunz, W., Garcia-Ruiz, J.M., 2013. The effect of silica on polymorphic precipitation of calcium carbonate: an on-line energy-dispersive X-ray diffraction (EDXRD) study. Nanoscale 5, 7054–7065.
Kleeberg, A., Herzog, C., Hupfer, M., 2013. Redox sensitivity of iron in phosphorus binding does not impede lake restoration. Water Res. 47, 1491–1502.
Kleiner, J., 1988. Coprecipitation of phosphate with calcite in lake water: a laboratory experiment modelling phosphorus removal with calcite in Lake Constance. Water Res. 22, 1259–1265.
Kraal, P., Slomp, C.P., Reed, D.C., Reichart, G.-J., Poulton, S.W., 2012. Sedimentary phosphorus and iron cycling in and below the oxygen minimum zone of the northern Arabian Sea. Biogeosciences 9, 2603–2624.
Kraal, P., van Genuchten, C.M., Behrends, T., Rose, A.L., 2019. Sorption of phosphate and silicate alters dissolution kinetics of poorly crystalline iron (oxyhydr)oxide. Chemosphere 234, 690–701.
Kraal, P., van Genuchten, C.M., Lenstra, W.K., Behrends, T., 2020. Coprecipitation of phosphate and silicate affects environmental iron (oxyhydr) oxide transformations: A gel-based diffusive sampler approach. Environ. Sci. Tech. 54, 12795–12802.
Luedecke, C., Hermanowicz, S.W., Jenkins, D., 1989. Precipitation of ferric phosphate in activated sludge: A chemical model and its verification. Water Sci. Technol. 21, 325–337.
Majzlan, J., 2011. Thermodynamic Stabilization of Hydrous Ferric Oxide by Adsorption of Phosphate and Arsenate. Environ. Sci. Tech. 45, 4726–4732.
Mao, Y., Ninh Pham, A., Xin, Y., Waite, T.D., 2012. Effects of pH, floc age and organic compounds on the removal of phosphate by pre-polymerized hydrous ferric oxides. Sep. Purif. Technol. 91, 38–45.
Mayer, D.T., Jarrell, W.M., 2000. Phosphorus sorption during iron(II) oxidation in the presence of dissolved silica. Water Res. 34, 3949–3956.
McLaughlin, J.R., Syers, J.K., 1978. Stability of ferric phosphates. J. Soil Sci. 29, 499–504.
Meinikmann, K., Hupfer, M., Lewandowski, J., 2015. Phosphorus in groundwater discharge–A potential source for lake eutrophication. J. Hydrol. 524, 214–226.
Mendez, J.C., Hiemstra, T., 2018. Carbonate adsorption to ferrihydrite: Competitive interaction with phosphate for use in soil systems. ACS Earth Space Chem. 3, 129–141.
Mendez, J.C., Hiemstra, T., 2020. Ternary Complex Formation of Phosphate with Ca and Mg Ions Binding to Ferrihydrite: Experiments and Mechanisms. ACS Earth Space Chem. 4, 545–557.
Merz-Preiß, M., Riding, R., 1999. Cyanobacterial tufa calcification in two freshwater streams: ambient environment, chemical thresholds and biological processes. Sed. Geol. 126, 103–124.
Mikutta, C., 2011. X-ray absorption spectroscopy study on the effect of hydroxybenzoic acids on the formation and structure of ferrihydrite. Geochim. Cosmochim. Acta 75, 5122–5139.
Millero, F., Huang, F., Zhu, X., Liu, X., Zhang, J.-Z., 2001. Adsorption and desorption of phosphate on calcite and aragonite in seawater. Aquat. Geochem. 7, 33–56.
Mort, H.P., Slomp, C.P., Gustafsson, B.G., Andersen, T.J., 2010. Phosphorus recycling and burial in Baltic Sea sediments with contrasting redox conditions. Geochim. Cosmochim. Acta 74, 1350–1362.
Notini, L., ThomasArrigo, L.K., Kaegi, R., Kretzschmar, R., 2022. Coexisting goethite promotes Fe (II)-catalyzed transformation of ferrihydrite to goethite. Environ. Sci. Tech. 56, 12723–12733.
Oelkers, E.H., Valsami-Jones, E., 2008. Phosphate mineral reactivity and global sustainability. Elements 4, 83–87.
Paige, C., Snodgrass, W., Nicholson, R.V., Scharer, J., He, Q., 1997. The effect of phosphate on the transformation of ferrihydrite into crystalline products in alkaline media. Water Air Soil Pollut. 97, 397–412.
Pain, A.J., Martin, J.B., Young, C.R., Valle-Levinson, A., Mariño-Tapia, I., 2020. Carbon and phosphorus processing in a carbonate karst aquifer and delivery to the coastal ocean. Geochim. Cosmochim. Acta 269, 484–495.
Paktunc, D., Dutrizac, J., Gertsman, V., 2008. Synthesis and phase transformations involving scorodite, ferric arsenate and arsenical ferrihydrite: implications for arsenic mobility. Geochim. Cosmochim. Acta 72, 2649–2672.
Parkhurst, D.L., Appelo., C.A.J, 1999. User's Guide to PHREEQC (Version 2): A Computer Program for Speciation, Batch-Reaction, One-Dimensional Transport, and Inverse Geochemical Calculations. U.S Geological Survey, Denver, CO.

Paytan, A., McLaughlin, K., 2007. The oceanic phosphorus cycle. Chem. Rev. 107, 563–576.
Pedersen, H.D., Postma, D., Jakobsen, R., Larsen, O., 2005. Fast transformation of iron oxyhydroxides by the catalytic action of aqueous Fe (II). Geochim. Cosmochim. Acta 69, 3967–3977.
Plant, L.J., House, W.A., 2002. Precipitation of calcite in the presence of inorganic phosphate. Colloids Surf. A Physicochem. Eng. Asp. 203, 143–152.
Ravel, B., Newville, M., 2005. ATHENA, ARTEMIS, HEPHAESTUS: data analysis for X-ray absorption spectroscopy using IFEFFIT. J. Synchrotron Radiat. 12, 537–541.
Reddy, M.M., 1977. Crystallization of calcium carbonate in the presence of trace concentrations of phosphorus-containing anions: I. Inhibition by phosphate and glycerophosphate ions at pH 8.8 and 25°C. J. Cryst. Growth 41, 287–295.
Roberts, L.C., Hug, S.J., Dittmar, J., Voegelin, A., Saha, G.C., Ali, M.A., Badruzzaman, A. B.M., Kretzschmar, R., 2007. Spatial distribution and temporal variability of arsenic in irrigatedrice fields in Bangladesh. 1. Irrigation water. Environ. Sci. Technol. 41, 5960–5966.
Sato, S., Solomon, D., Hyland, C., Ketterings, Q.M., Lehmann, J., 2005. Phosphorus speciation in manure and manure-amended soils using XANES spectroscopy. Environ. Sci. Tech. 39, 7485–7491.
Schwertmann, U., Carlson, L., Fechter, H., 1984. Iron oxide formation in artificial ground waters. Schweiz. Zeitschr. Hydrol. 46, 185–191.
Schwertmann, U., Fechter, H., 1994. The formation of green rust and its transformation to lepidocrocite. Clay Miner. 29, 87–92.
Schwertmann, U., Taylor, R., 1979. Natural and synthetic poorly crystallized lepidocrocite. Clay Miner. 14, 285–293.
Schwertmann, U., Thalmann, H., 1976. The influence of [Fe (II)],[Si], and pH on the formation of lepidocrocite and ferrihydrite during oxidation of aqueous $FeCl_2$ solutions. Clay Miner. 11, 189–200.
Senn, A.C., Hug, S.J., Kaegi, R., Hering, J.G., Voegelin, A., 2018. Arsenate co-precipitation with Fe(II) oxidation products and retention or release during precipitate aging. Water Res. 131, 334–345.
Senn, A.-C., Kaegi, R., Hug, S.J., Hering, J.G., Mangold, S., Voegelin, A., 2015. Composition and structure of Fe(III)-precipitates formed by Fe(II) oxidation in near-neutral water: Interdependent effects of phosphate, silicate and Ca. Geochim. Cosmochim. Acta 162, 220–246.
Senn, A.-C., Kaegi, R., Hug, S.J., Hering, J.G., Mangold, S., Voegelin, A., 2017. Effect of aging on the structure and phosphate retention of Fe(III)-precipitates formed by Fe (II) oxidation in water. Geochim. Cosmochim. Acta 202, 341–360.
Shannon, R.D., 1976. Revised effective ionic radii and systematic studies of interatomic distances in halides and chalcogenides. Acta Crystallogr. A 32, 751–767.
Sheng, A., Liu, J., Li, X., Qafoku, O., Collins, R.N., Jones, A.M., Pearce, C.I., Wang, C., Ni, J., Lu, A., Rosso, K.M., 2020. Labile Fe(III) from sorbed Fe(II) oxidation is the key intermediate in Fe(II)-catalyzed ferrihydrite transformation. Geochim. Cosmochim. Acta 272, 105–120.
Slomp, C.P., Van Cappellen, P., 2004. Nutrient inputs to the coastal ocean through submarine groundwater discharge: controls and potential impact. J. Hydrol. 295, 64–86.
Smith, V.H., Tilman, G.D., Nekola, J.C., 1999. Eutrophication: impacts of excess nutrient inputs on freshwater, marine, and terrestrial ecosystems. Environ. Pollut. 179–196.
Sø, H.U., Postma, D., Jakobsen, R., Larsen, F., 2011. Sorption of phosphate onto calcite; results from batch experiments and surface complexation modeling. Geochim. Cosmochim. Acta 75, 2911–2923.
Sundman, A., Karlsson, T., Sjöberg, S., Persson, P., 2016. Impact of iron–organic matter complexes on aqueous phosphate concentrations. Chem. Geol. 426, 109–117.
Swedlund, P.J., Miskelly, G.M., McQuillan, A.J., 2010. Silicic acid adsorption and oligomerization at the ferrihydrite-water interface: interpretation of ATR-IR spectra based on a model surface structure. Langmuir 26, 3394–3401.
Swedlund, P.J., Sivaloganathan, S., Miskelly, G.M., Waterhouse, G.I.N., 2011. Assessing the role of silicate polymerization on metal oxyhydroxide surfaces using X-ray photoelectron spectroscopy. Chem. Geol. 285, 62–69.
Taylor, K.G., Konhauser, K.O., 2011. Iron in earth surface systems: A major player in chemical and biological processes. Elements 7, 83–88.
Thibault, P.-J., Rancourt, D.G., Evans, R.J., Dutrizac, J.E., 2009. Mineralogical confirmation of a near-P:Fe=1:2 limiting stoichiometric ratio in colloidal P-bearing ferrihydrite-like hydrous ferric oxide. Geochim. Cosmochim. Acta 73, 364–376.
ThomasArrigo, L.K., Mikutta, C., Byrne, J., Barmettler, K., Kappler, A., Kretzschmar, R., 2014. Iron and arsenic speciation and distribution in organic flocs from streambeds of an arsenic-enriched peatland. Environ. Sci. Tech. 48, 13218–13228.
Valsami-Jones, E., 2001. Mineralogical controls on phosphorus recovery from wastewaters. Mineral. Mag. 65, 611–620.
van der Grift, B., Behrends, T., Osté, L.A., Schot, P.P., Wassen, M.J., Griffioen, J., 2016. Fe hydroxyphosphate precipitation and Fe(II) oxidation kinetics upon aeration of Fe (II) and phosphate-containing synthetic and natural solutions. Geochim. Cosmochim. Acta 186, 71–90.
Van Der Houwen, J.A., Valsami-Jones, E., 2001. The application of calcium phosphate precipitation chemistry to phosphorus recovery: the influence of organic ligands. Environ. Technol. 22, 1325–1335.
van Genuchten, C.M., Gadgil, A.J., Peña, J., 2014a. Fe(III) nucleation in the presence of bivalent cations and oxyanions leads to subnanoscale 7 Å polymers. Environ. Sci. Tech. 48, 11828–11836.
van Genuchten, C.M., Peña, J., Amrose, S.E., Gadgil, A.J., 2014b. Structure of Fe(III) precipitates generated by the electrolytic dissolution of Fe(0) in the presence of groundwater ions. Geochim. Cosmochim. Acta 127, 285–304.
Villalobos, M., Leckie, J.O., 2001. Surface complexation modeling and FTIR study of carbonate adsorption to goethite. J. Colloid Interface Sci. 235, 15–32.
Violante, A., Gaudio, S.D., Pigna, M., Ricciardella, M., Banerjee, D., 2007. Coprecipitation of arsenate with metal oxides. 2. Nature, mineralogy, and reactivity of iron (III) precipitates. Environ. Sci. Tech. 41, 8275–8280.
Voegelin, A., Kaegi, R., Frommer, J., Vantelon, D., Hug, S.J., 2010. Effect of phosphate, silicate, and Ca on Fe(III)-precipitates formed in aerated Fe(II)- and As(III)-containing water studied by X-ray absorption spectroscopy. Geochim. Cosmochim. Acta 74, 164–186.
Voegelin, A., Senn, A.-C., Kaegi, R., Hug, S.J., Mangold, S., 2013. Dynamic Fe-precipitate formation induced by Fe(II) oxidation in aerated phosphate-containing water. Geochim. Cosmochim. Acta 117, 216–231.
Wang, L., Nancollas, G.H., 2008. Calcium orthophosphates: crystallization and dissolution. Chem. Rev. 108, 4628–4669.
Wang, Z., Xiao, D., Bush, R.T., Liu, J., 2015. Coprecipitated arsenate inhibits thermal transformation of 2-line ferrihydrite: implications for long-term stability of ferrihydrite. Chemosphere 122, 88–93.
Wolthoorn, A., Temminghoff, E.J., Weng, L., van Riemsdijk, W.H., 2004. Colloid formation in groundwater: effect of phosphate, manganese, silicate and dissolved organic matter on the dynamic heterogeneous oxidation of ferrous iron. Appl. Geochem. 19, 611–622.
Wright, K.E., Hartmann, T., Fujita, Y., 2011. Inducing mineral precipitation in groundwater by addition of phosphate. Geochem. Trans. 12 (8), 1–13.